

# SARS-CoV-2 Nsp6 causes cardiac defects through MGA/MAX complex-mediated increased glycolysis

Jun-yi Zhu

Guanglei Wang

Xiaohu Huang

Hangnoh Lee

Jin-Gu Lee

Penghua Yang

Joyce van de Leemput

<https://orcid.org/0000-0003-1903-7295>

Weiliang Huang

Maureen Kane

Peixin Yang

University of Maryland School of Medicine <https://orcid.org/0000-0002-2104-0699>

Zhe Han (✉ [ZHan@som.umaryland.edu](mailto:ZHan@som.umaryland.edu))

University of Maryland Baltimore <https://orcid.org/0000-0002-5177-7798>

---

## Article

**Keywords:** Drosophila, SARS-CoV-2, Nsp6, MGA, MAX, MYC, glycolysis, cardiac pathology

**Posted Date:** June 6th, 2022

**DOI:** <https://doi.org/10.21203/rs.3.rs-1677754/v1>

**License:** © ⓘ This work is licensed under a Creative Commons Attribution 4.0 International License.

[Read Full License](#)

---

**Version of Record:** A version of this preprint was published at Communications Biology on September 30th, 2022. See the published version at <https://doi.org/10.1038/s42003-022-03986-6>.

1 **SARS-CoV-2 Nsp6 causes cardiac defects through MGA/MAX complex-**  
2 **mediated increased glycolysis**

3

4 Jun-yi Zhu<sup>1,2</sup>, Guanglei Wang<sup>3</sup>, Xiaohu Huang<sup>1,2</sup>, Hangnoh Lee<sup>1,2</sup>, Jin-Gu  
5 Lee<sup>1,2</sup>, Penghua Yang<sup>3</sup> Joyce van de Leemput<sup>1,2</sup>, Weiliang Huang<sup>4</sup>, Maureen  
6 A. Kane<sup>4</sup>, Peixin Yang<sup>3</sup>, Zhe Han<sup>1,2\*</sup>

7

8 **Author affiliations:**

9 1 Center for Precision Disease Modeling, Department of Medicine, University  
10 of Maryland School of Medicine, 670 West Baltimore Street, Baltimore, MD,  
11 21201 USA

12 2 Division of Endocrinology, Diabetes and Nutrition, Department of Medicine,  
13 University of Maryland School of Medicine, 670 West Baltimore Street,  
14 Baltimore, MD, 21201 USA

15 3 Department of Obstetrics, Gynecology & Reproductive Sciences, University  
16 of Maryland School of Medicine, Baltimore, MD, 21201 USA

17 4 Department of Pharmaceutical Sciences, University of Maryland School of  
18 Pharmacy, Baltimore, MD, 21201 USA

19 \* Corresponding author email: zhan@som.umaryland.edu

20

21 **Short title:** Nsp6 induces glycolysis affecting the heart

22

23 **Keywords:** *Drosophila*, SARS-CoV-2, Nsp6, MGA, MAX, MYC, glycolysis,  
24 cardiac pathology

25

26 **SUMMARY**

27

28 SARS-CoV-2 infection causes COVID-19, a severe acute respiratory disease  
29 associated with cardiovascular complications including long-term outcomes.

30 The presence of virus in cardiac tissue of patients with COVID-19 suggests this  
31 is a direct, rather than secondary, effect of infection. By expressing individual  
32 SARS-CoV-2 proteins in the *Drosophila* heart we demonstrated interaction of  
33 virus Nsp6 with host proteins of the MGA/MAX complex (MGA, PCGF6 and  
34 TFDP1). Complementing transcriptomic data from the fly heart revealed that  
35 this interaction blocks the antagonistic MGA/MAX complex, which shifts the  
36 balance towards MYC/MAX and activates glycolysis—with similar findings in  
37 mouse cardiomyocytes. Further, the Nsp6-induced glycolysis disrupted cardiac  
38 mitochondrial function, known to increase reactive oxygen species (ROS) in  
39 heart failure; this could explain COVID-19-associated cardiac pathology.  
40 Furthermore, inhibiting the glycolysis pathway by 2-deoxy-D-glucose (2DG)  
41 treatment attenuated the Nsp6-induced cardiac phenotype in fly and mice; thus,  
42 suggesting glycolysis as a potential pharmacological target for treating COVID-  
43 19-associated heart failure.

44

45

46

47

48

49 **INTRODUCTION**

50

51 COVID-19, the disease caused by SARS-CoV-2 infection, is notable for its wide  
52 range in severity; from asymptomatic to severe acute respiratory syndrome,  
53 systemwide organ failure and ultimately death. Similarly, while COVID-19 is  
54 known as a severe acute respiratory syndrome (SARS), it presents with a wide  
55 variety of symptoms that often include cardiac pathology. The detection of  
56 SARS-CoV-2 in cardiac tissue (Escher *et al.*, 2020; Lindner *et al.*, 2020; Tavazzi  
57 *et al.*, 2020; Dal Ferro *et al.*, 2021; D’Onofrio *et al.*, 2021; Bräuninger *et al.*,  
58 2022; Kogan *et al.*, 2022), suggests the cardiac pathology is caused by direct  
59 virus action, rather than secondary complications. Notably, elevated levels of  
60 cardiac biomarkers—such as, troponins, myoglobin, C-reactive protein,  
61 interleukins and natriuretic peptides—indicative of myocardial injury, have been  
62 observed in COVID-19 (Bielecka-Dabrowa *et al.*, 2021). Their presence,  
63 combined with abnormal echocardiograms that reflect functional deficits, has  
64 been associated with a poorer prognosis of disease progression (Dweck *et al.*,  
65 2020; Guo *et al.*, 2020; Shi *et al.*, 2020). Indeed, cardiovascular complications  
66 reported in COVID-19 patients include necrosis, ventricular dysfunction heart  
67 failure, and arrhythmia (Bielecka-Dabrowa *et al.*, 2021). Moreover, there is  
68 evidence of myocardial inflammation (myocarditis) following SARS-CoV-2  
69 infection, including in asymptomatic individuals (Puntmann *et al.*, 2020; Rajpal  
70 *et al.*, 2021); and, the long-term (1-year) risk of cardiovascular disease is  
71 considerable in COVID-19 patients, independent of hospitalization (Xie *et al.*,  
72 2022).

73

74 The key to treating the SARS-CoV-2 induced cardiovascular pathology likely  
75 lies in understanding and targeting the individual virus-host interactions (van de  
76 Leemput and Han, 2021b). Initially these have been investigated in large-scale  
77 network studies which revealed distinct proteome interaction networks, for  
78 many of these interactions specific pharmacological compounds exist (Gordon,  
79 Hiatt, *et al.*, 2020; Gordon, Jang, *et al.*, 2020; Guzzi *et al.*, 2020; Parkinson *et*  
80 *al.*, 2020; Belyaeva *et al.*, 2021; Gaziano *et al.*, 2021; Li *et al.*, 2021). Of these  
81 compounds, numerous are currently being tested in clinical trials for their  
82 efficacy in treating COVID-19. More recently, studies have been published that  
83 delve deeper into the individual SARS-CoV-2 proteins, their host interactions  
84 and underlying pathomechanisms. These have already revealed that some  
85 virus proteins known for their role in virus replication processes, such as SARS-  
86 CoV-2 Nsp3 and Nsp5 which encode the (PLpro) and (3CL pro; main protease,  
87 Mpro), are also responsible for disrupting host immune signaling processes  
88 through specific protein-protein interactions (Shin *et al.*, 2020; Moustaqil *et al.*,  
89 2021). These findings suggest that therapeutics targeting these virus proteins  
90 specifically could both reduce virus replication and diminish their role in the  
91 damaging host pathogenic effects.

92

93 Viruses often take control of host metabolic processes to support virus  
94 replication (Drucker, 2021; Ho *et al.*, 2021). These metabolic and signaling  
95 pathways are highly conserved, and studies in *Drosophila* have led to the  
96 discovery of several of these systems, preceding their identification in  
97 mammalian species (Singh and Irvine, 2012). As such, the fly has proven  
98 valuable in the study of virus-host interaction and related pathogenic

99 mechanisms for a variety of human viruses, including human immunodeficiency  
100 virus (HIV), Zika virus (ZIKV), and dengue virus to name but a few (Hughes *et*  
101 *al.*, 2012; Harnish, Link and Yamamoto, 2021; van de Leemput and Han,  
102 2021a); and, the fly has been used to study specific coronavirus proteins and  
103 their pathogenic effects on host cells. For example, overexpression of SARS-  
104 CoV Orf3a or membrane (M) proteins caused cytotoxicity in the fly eye (Wong  
105 *et al.*, 2005; Chan *et al.*, 2007). Moreover, *Drosophila* forward genetic screens  
106 were used to identify host genetic modifiers of these pathogenic virus-host  
107 protein interactions. Notably, nearly 60% of the modifiers identified in these fly  
108 studies have human orthologs that are expressed in lung tissue (Wong *et al.*,  
109 2005; Chan *et al.*, 2007). And a recent publication by our group identified  
110 SARS-CoV-2 Orf6, Nsp6 and Orf7a to be most pathogenic when expressed in  
111 fly (Zhu *et al.*, 2021). Further study revealed damage to muscle, characterized  
112 by reduced mitochondria, and abnormal trachea (fly equivalent of human lung).  
113 Interestingly, treatment with selinexor, a compound known to target XPO1, the  
114 human host protein interacting with SARS-CoV-2 Orf6 protein, successfully  
115 attenuated the Orf6-induced phenotypes. However, selinexor was unable to  
116 treat the highly similar phenotypes induced by SARS-Cov-2 Orf7a or Nsp6,  
117 suggesting the underlying pathomechanism is specific to each virus protein.  
118 The relevance of these studies is evident in the extremely high level of  
119 conservation of the virus-host interactome, with 90% of human proteins in the  
120 SARS-CoV-2 protein interaction network conserved from flies (Hussain *et al.*,  
121 2020; Zhu *et al.*, 2021).

122

123 Altogether, the fruit fly makes a remarkably powerful and versatile model  
124 system. It combines the speed and versatility of *in vitro* models with the whole-  
125 body physiology (access to all major organs and tissues) of *in vivo* models.  
126 Despite the initial obvious differences, at the core flies and mammalian  
127 organisms share many molecular and biological systems. As such, flies have  
128 been instrumental in studying a variety of human diseases including  
129 developmental (congenital heart disease) and metabolic (diabetic  
130 cardiomyopathy) heart disorders. This is made possible by the *Drosophila* heart  
131 tube resembling the earliest stages of mammalian cardiac development, and  
132 due to the high level of conservation of key metabolic processes and regulatory  
133 mechanisms, including the lipid and glucose pathways (Diop and Bodmer,  
134 2015). Conservation of these systems is even observed when studying the  
135 effects of age, high fat diet, and the associated increased levels of reactive  
136 oxygen species (ROS) on heart function

137

138 Here we used *Drosophila* to study the effect of individual SARS-CoV-2 proteins  
139 on the heart. Findings revealed that expression of *Nsp6* specifically in the fly  
140 heart causes significant structural and functional damage, in resemblance of  
141 the myocardial injury and functional abnormalities observed in COVID-19  
142 patients. Furthermore, the data show this is mediated by direct interaction of  
143 *Nsp6* with the MGA/PCGF6/TFDP1/MAX [polycomb repressive complex 1.6  
144 (PRC1.6)] regulatory complex for glycolysis activity. Data from mouse  
145 cardiomyocytes confirmed the SARS-CoV-2 *Nsp6*-induced glycolysis and  
146 cardiac distress. Through this host interaction, *Nsp6* shifts the balance towards  
147 MYC/MAX regulation, thus leading to increased glycolysis and the observed

148 heart phenotype. These findings support a role for dysregulated glycolysis in  
149 COVID-19, specifically in heart pathology. Inhibition of glycolysis by treatment  
150 with 2-deoxy-D-glucose (2DG) largely attenuated the Nsp6-induced heart  
151 phenotype in flies and mice. Thus, identifying the glycolysis pathways as a  
152 therapeutic target for SARS-CoV-2 instigated heart failure in COVID-19  
153 patients.

154

155

## 156 **RESULTS**

157

### 158 **Heart-specific expression of individual SARS-CoV-2 transgenes causes** 159 **developmental lethality and a reduced lifespan**

160 Previously, we have generated transgenic fly lines each expressing an  
161 individual SARS-CoV-2 gene encoding one of the 12 virus proteins most likely  
162 to instigate pathogenic host interactions (Zhu *et al.*, 2021). SARS-CoV-2  
163 infection can progress to COVID-19, which is characterized by multiple cardiac  
164 manifestations. To understand how SARS-CoV-2 causes heart damage, we  
165 decided to use the heart-specific driver *4XHand-Gal4* to directly express these  
166 12 SARS-CoV-2 genes in the *Drosophila* heart and then study their pathogenic  
167 outcomes on cardiac structure and function.

168

169 Male and female flies of the designated genotypes were crossed to produce  
170 progeny carrying the corresponding UAS-SARS-CoV-2 gene construct, either  
171 with heart-specific expression of the individual virus gene driven by *4XHand-*  
172 *Gal4* (straight wing), or with the balancer (*CyO*, curly wing) (Figure 1A). We

173 found the expression of SARS-CoV-2 *Nsp6*, *Orf6* or *Orf7a* in the fly heart  
174 induced a high mortality rate, while *Nsp3* flies showed a mildly increased  
175 mortality rate (Figure 1B; Supplemental Figure S1). For the adult flies that  
176 eclosed, their lifespans were monitored. We found *Nsp6* expression in the fly  
177 heart caused a shortened lifespan as all flies died by 40 days, whereas control  
178 flies lived up to 70 days (Figure 1C). Flies with cardiac expression of *Orf6* or  
179 *Orf7a* showed a shortened lifespan as well, living a maximum of 50 days (Figure  
180 1C). These results suggest that these SARS-CoV-2 encoded proteins (*Nsp6*,  
181 *Orf6*, *Orf7a* and *Nsp3*) may be associated with cardiac pathology, with *Nsp6*  
182 having the most damaging effect in our model.

183

#### 184 **Heart-specific expression of the SARS-CoV-2 *Nsp6* transgene causes** 185 **heart morphological and functional defects**

186 To better understand the extent of individual SARS-CoV-2 *Nsp6*-induced heart  
187 damage, we first investigated if there were any morphological changes in the  
188 *Drosophila* heart. The fly hearts were stained with phalloidin to visualize the  
189 structure of the cardiac actin filaments (myofibrils). Heart-specific expression of  
190 *Nsp6* caused disorganized cardiac actin filaments and significantly reduced  
191 cardiac muscle fiber density (Figure 1D and E). Next, we applied optical  
192 coherence tomography (OCT) to assess any cardiac functional defects induced  
193 by heart-specific expression of *Nsp6*. The cardiac diastolic and systolic  
194 diameter, and the heart period were measured to determine cardiac function  
195 (Figure 1F and G). We found that *Nsp6* expression reduced the diastolic (Figure  
196 1H)—but not the systolic (*data not shown*)—diameter of the heart tube.  
197 Furthermore, *Nsp6* expression significantly affected the heart period (*i.e.*

198 reduced heart rate) (Figure 1I). These results indicate that SARS-CoV-2 *Nsp6*  
199 can induce heart structural damage and cardiac functional defects.

200

### 201 **Glycolysis genes are upregulated in the SARS-CoV-2 *Nsp6* transgenic fly** 202 **hearts**

203 To gain insight into the mechanism underlying the cardiac phenotype, we  
204 performed RNAseq analysis of the dissected fly hearts that specifically  
205 expressed SARS-CoV-2 *Nsp6* (Supplemental Table S1). The differential gene  
206 expression profile revealed significantly increased expression of carbon  
207 metabolism genes (Figure 2A; adj. P value < 0.05, Wald test, corrected with  
208 Benjamini-Hochberg method). For example, *Ald* gene encodes Aldolase, a key  
209 enzyme in glycolysis that converts Fructose 1,6-bisphosphate into two triose  
210 phosphates, Dihydroxyacetone phosphate and Glyceraldehyde 3-phosphate  
211 (Perham, 1990); *Ald* was upregulated 2.68 times in fly hearts with *Nsp6*  
212 expression (adj. P = 4.84e-13). Similarly, genes encoding proteins upstream of  
213 Ald in the glycolytic pathway, such as Hex-C (Hexokinase C, 2.55 fold, adj. P =  
214 4.04e-06) and Pgi (Phosphoglucose isomerase, 2.45 fold, adj. P = 2.23e-08),  
215 as well as downstream of it, PyK (Pyruvate kinase, 2.13 fold, adj. P = 1.7e-07),  
216 showed increased expression in the *Nsp6* expressing fly hearts. In addition, we  
217 observed a significant increase of *CG32444* expression (6.15 fold, adj. P =  
218 5.11e-20), which encodes an ortholog of human GALM (Galactose  
219 mutarotase). This protein is not a core member of glycolysis, but its function is  
220 required for the utilization of galactose via glycolysis (Sellick, Campbell and  
221 Reece, 2008).

222

223 The differential expression of multiple glycolytic genes in response to SARS-  
224 CoV-2 *Nsp6*, could reflect altered steps in cellular respiration or carbon  
225 metabolism. To test this, we subdivided the metabolic genes into four groups  
226 based on their classification in KEGG (Kyoto Encyclopedia of Genes and  
227 Genomes) (Kanehisa *et al.*, 2021). Genes involved in glycolysis showed greater  
228 upregulation (median = 1.84 fold), than those encoding proteins in the  
229 tricarboxylic acid cycle (TCA, median = 1.25 fold,  $P = 0.0039$ , Mann–Whitney  
230 U test) or oxidative phosphorylation (OxPhos, median = 1.32 fold,  $P = 7.389e$ -  
231 09) (Figure 2B and C). Glycolysis is tightly linked to the pentose phosphate  
232 pathway (PPP). It has been postulated that enhanced glycolysis and PPP are  
233 beneficial for viral replication by providing PPP intermediates for the nucleotide  
234 precursors (Vastag *et al.*, 2011). Consistent with this idea, we found that *Nsp6*  
235 expression led to PPP gene upregulation (median = 2.01 fold). This  
236 upregulation was comparable in scope to the upregulation of the glycolysis  
237 genes (median = 1.84 fold) following *Nsp6* expression ( $P = 0.96$ ; *i.e.* no  
238 significant difference between PPP and glycolysis gene upregulation in *Nsp6*  
239 flies). Interestingly, the *Drosophila* glycolysis pathway genes are highly  
240 conserved from fly to human based on their ortholog conservation scores  
241 (DIOPT; Figure 2C).

242

243 Pathway analysis further supported our findings and demonstrated over-  
244 representation of carbon metabolism, especially glycolysis-related, genes  
245 among the upregulated genes (Figure 2D and E). Gene Ontology (GO) analysis  
246 showed enrichment of functional terms linked to the oxoacid metabolic process  
247 (adj.  $P = 3.94e-21$ , Hypergeometric test, corrected with Benjamini-Hochberg

248 method), carboxylic acid metabolic process (adj.  $P = 7.27e-21$ ), and  
249 carbohydrate metabolic process (adj.  $P = 1.46e-24$ ) (Figure 2D). KEGG  
250 pathway analysis provided deeper understanding of the specific carbon  
251 metabolism pathways affected by *Nsp6*. It showed that genes involved in  
252 glycolysis/gluconeogenesis (adj.  $P = 5.21e-9$ ) and PPP (adj.  $P = 7.29e-6$ ) were  
253 significantly enriched among the upregulated genes (Figure 2E).

254

255 Altogether, these findings indicate SARS-CoV-2 *Nsp6*-mediated upregulation  
256 of glycolysis might contribute to the observed cardiac defect in flies and given  
257 the high level of conservation, possibly in COVID-19 patients as well.

258

259 **SARS-CoV-2 *Nsp6*-induced glycolysis and increased Pgi are associated**  
260 **with heart morphological and functional defects**

261 The gene expression data indicated SARS-CoV-2 *Nsp6* induced glycolysis, we  
262 wanted to validate this finding with a biochemical assay. Therefore, we  
263 quantified the activity of Pgi, Phosphoglucose isomerase, a key enzyme at the  
264 start of the glycolysis pathway that interconverts Glucose-6-phosphate and  
265 Fructose-6-phosphate (Figure 3A). The assay confirmed that ubiquitous  
266 expression of SARS-CoV-2 *Nsp6* significantly increases Pgi activity (Figure  
267 3A). In addition, we measured NADH levels, a metabolite produced from NAD<sup>+</sup>  
268 through glycolysis. Similarly, NADH levels significantly increased following  
269 ubiquitous expression of *Nsp6* in flies (Figure 3A). Combined, the RNAseq gene  
270 expression and biochemical assay data provide demonstrate that SARS-CoV-  
271 2 *Nsp6* can induce glycolysis.

272

273 Glycolysis take place in the cytoplasm and generates energy, in the form of  
274 ATP, by converting glucose into pyruvate. Under aerobic conditions, pyruvate  
275 can diffuse into the mitochondria, enter the citric acid cycle and generate  
276 additional ATP. Therefore, we next tested if the increased glycolysis observed  
277 in flies with heart-specific SARS-CoV-2 *Nsp6* could disrupt the cardiac  
278 mitochondria, either indirectly via *Nsp6* or directly via the glycolysis pathway  
279 enzyme *Pgi*. Therefore, we genetically overexpressed either *Nsp6* or *Pgi* (using  
280 the heart-specific *4XHand* driver) and investigated their impact on mitochondria  
281 in the *Drosophila* heart. We found both *Nsp6* and *Pgi* overexpression caused  
282 disorganization of the cardiac actin filaments, and significant loss of  
283 mitochondria activity as visualized by ATP5a (Figure 3B and C). These results  
284 indicate that increased glycolysis pathway activity can lead to mitochondrial  
285 defects causing heart damage.

286

287 Finally, we assessed if increased glycolysis by itself could induce a cardiac  
288 phenotype like that caused by heart-specific expression of SARS-CoV-2 *Nsp6*  
289 in fly. We genetically overexpressed *Pgi* (heart-specific using the *4XHand*  
290 driver) to investigate the effect on *Drosophila* heart morphology and function.  
291 We found *Pgi* overexpression induced a high mortality rate (29.5%) compared  
292 to control flies (*data not shown*). In the *4XHand*-driven *Pgi* flies that did emerge  
293 as adults, we found *Pgi* caused disorganized cardiac actin filaments and  
294 reduced cardiac muscle fiber density (Figure 3B). In addition, OCT imaging  
295 revealed heart-specific *Pgi* overexpression led to reduced heart diastolic  
296 diameter and a lengthened heart period, *i.e.* reduced heart rate (Figure 3D, E  
297 and F). These results indicate that increased glycolysis pathway activity can

298 lead to heart damage, both structurally and functionally.

299

300 **SARS-CoV-2 Nsp6 interacts with MGA and the non-canonical polycomb**  
301 **repressive complex**

302 To identify how glycolysis genes are upregulated and cause the physiological  
303 differences upon SARS-CoV-2 *Nsp6* expression, we performed mass  
304 spectrometry analysis using human HEK 293T cells that ectopically express  
305 mCherry and FLAG-tagged *Nsp6*. A total of 661 proteins were uniquely  
306 detected in the *Nsp6* expressing cells, *i.e.* proteins without any detectable  
307 pulldown in the control cells (Supplemental Table S2). Next, to uncover which  
308 transcription factors might regulate the underlying transcriptomic changes, and  
309 thus are likely the intermediates affected by SARS-CoV-2 *Nsp6*, we compared  
310 the 661 *Nsp6* binding proteins against a list of 1,639 human transcription factors  
311 (Lambert *et al.*, 2018). This identified nine transcription factors unique to *Nsp6*  
312 expressing cells (Figure 4A), suggesting SARS-CoV-2 *Nsp6* interacts with  
313 these transcription factors to instigate transcriptomic changes that favor the  
314 virus.

315

316 Intriguingly, among the nine transcription factors, three (MGA, PCGF6 and  
317 TFDP1) are part of the non-canonical PRC1.6 complex (Stielow *et al.*, 2018)  
318 (Figure 4B). PRCs are polycomb repressive complexes that play major roles in  
319 gene regulation, differentiation, cell cycle control, and development and are  
320 known for their varied subunit composition. PRC1.6 specifically is made up of  
321 PCGF6 (Polycomb group RING finger protein 6), MGA (MAX gene-associated  
322 protein) and E2F6 transcription factors, and L3MBTL2 (a histone-binding

323 protein) (Stielow *et al.*, 2018). PCGF6 is the defining subunit of this particular  
324 PRC, while MGA was shown essential for targeting specific genomic sites as a  
325 sequence-specific DNA-binding factor and through its scaffolding function  
326 (Stielow *et al.*, 2018). E2F6 (Transcription factor E2F6) and TFDP1  
327 (Transcription factor Dp-1) form a dimer involved in gene repression (Llabata  
328 *et al.*, 2020). MGA regulates MYC-MAX target gene expression by suppressing  
329 transcriptional activation by MYC (Llabata *et al.*, 2020). In fact, both MGA and  
330 MYC partner with MAX and both recognize the same sequence (E-box DNA-  
331 motif) resulting in antagonistic action, *i.e.* the genes targeted, bound and  
332 activated by MYC, are bound and repressed by MGA (Figure 4B and C).  
333 Notably, MGA/PCGF6/TFDP1/MAX:MYC/MAX regulated genes include those  
334 important for the G<sub>2</sub>-M checkpoint in the cell cycle and for glycolysis (Llabata *et*  
335 *al.*, 2020). Based on these previous findings, we hypothesized SARS-CoV-2  
336 Nsp6 blocks the PRC1.6 complex (which comprises MGA/MAX) through  
337 interaction with multiple complex proteins (MGA, PCGF6 and TFDP1) thus  
338 releasing its antagonistic effect on MYC/MAX, thereby inducing translation of  
339 MYC-pathway target genes which also encode proteins important for glycolysis.  
340 To confirm the link between increased MYC and increased glycolysis activity,  
341 we ubiquitously overexpressed *Myc*, the fly homolog of human *MYC*, and  
342 assayed glycolysis pathway components. *Myc* overexpression significantly  
343 increased the activity of Pgi (Figure 4D) as well as the level of NADH (Figure  
344 4E) in flies. These findings are similar to the SARS-CoV-2 *Nsp6*-induced  
345 dysregulation of glycolysis and suggest that disruption of the  
346 MGA/MAX:MYC/MAX balance might act as the *Nsp6* mediator in this process.  
347

348 **Inhibition of glycolysis pathway activity by 2-deoxy-D-glucose (2DG)**  
349 **attenuates SARS-CoV-2 Nsp6-induced heart morphological and**  
350 **functional defects**

351 Next, we investigated means of pharmacological intervention of the *Nsp6*-  
352 induced glycolysis increase and related phenotypes. The compound 2-deoxy-  
353 D-glucose (2DG) is a known inhibitor of glycolysis pathway activity by targeting  
354 hexokinase and Pgi (Wick *et al.*, 1957; Sottnik *et al.*, 2011; Pajak *et al.*, 2019).  
355 Therefore, we tested whether treating the flies with 2DG could attenuate the  
356 *Nsp6*-induced cardiac defects. Starting at the 1<sup>st</sup> instar larval stage, the flies  
357 were administered different doses of 2DG (0, 2, 10, 50 mM) through their food.  
358 A 50 mM dose 2DG turned out to be toxic to the flies resulting in near complete  
359 lethality across control and *Nsp6*-transgenic flies (Figure 5A). The 2 mM dose  
360 of 2DG had no detectable effect in either control or *Nsp6*-transgenic flies.  
361 However, the 10mM dose significantly attenuated *Nsp6*-induced mortality  
362 (Figure 5A) as well as heart morphological (Figure 5B and C) and functional  
363 defects (Figure 5D and E). This dose caused a slight, yet significant, increase  
364 in mortality in the control flies, but had no significant effect on heart morphology  
365 or function in these flies. Taken together, these results further strengthen the  
366 link between SARS-CoV-2 *Nsp6* protein, MYC-pathway dysregulation,  
367 increased glycolysis and ultimately cardiac damage.

368

369 Finally, we determined whether our findings in fly translated to a mammalian  
370 model. We isolated primary cardiomyocytes from E12.5 mice embryonic heart  
371 and transfected the cell cultures with the *SARS-CoV-2 Nsp6* transgene (Figure  
372 6A). Mice in which glucose metabolism has been disrupted frequently show

373 hypertrophy within their cardiac phenotype (Tran and Wang, 2019), therefore  
374 we checked our cardiomyocytes for hypertrophy. We found SARS-CoV-2 *Nsp6*  
375 (*Nsp6*-OE) significantly increased Atrial natriuretic peptide (ANP) and type B  
376 natriuretic peptide (BNP), both established markers of cardiac hypertrophy,  
377 compared to primary cardiomyocytes from the control group (Lipofectamine;  
378 Lipo) (Figure 6B). Moreover, the relative expression level of genes involved in  
379 glycolysis (*Gpi1*, *Pfkm*, *Pgam2*, and *Eno1*) were significantly increased after  
380 *Nsp6*-OE (Figure 6C); and like in fly, these could be restored by 2DG  
381 supplementation (Figure 6C). Primary cardiomyocytes with SARS-CoV-2 *Nsp6*-  
382 OE exhibited significantly lower contraction rates (mimicking a heartbeat; *data*  
383 *not shown*) as well as increased Ca<sup>2+</sup> absorption intervals when compared to  
384 the control cultures (Lipo) (Figure 6D and E). Supplementation with 2DG  
385 restored the Ca<sup>2+</sup> absorption by significantly lowering the intervals in *Nsp6*-OE  
386 primary cardiomyocytes (Figure 6D and E). Together, these results confirmed  
387 that SARS-CoV-2 *Nsp6* significantly affects mouse heart function by regulating  
388 the glycolysis pathway, as inhibition of glycolysis pathway activity with 2DG  
389 significantly attenuated the cardiomyocyte phenotype.

390

391

## 392 **DISCUSSION**

393

### 394 **SARS-CoV-2 *Nsp6*-induced glycolysis in cardiac pathology**

395 Cardiovascular complications are widely observed in COVID-19. In fact,  
396 increased levels of biomarkers for cardiac injury and abnormal  
397 echocardiograms (heart rhythmic function) frequently occur in COVID-19

398 patients (Szekely *et al.*, 2020; Bader *et al.*, 2021)—even prior to cardiac  
399 symptomatology and in those infected but otherwise asymptomatic (Puntmann  
400 *et al.*, 2020; Rajpal *et al.*, 2021). The metabolic pathways that regulate heart  
401 development and function, including glycolysis, are highly conserved from fly to  
402 human (Cammarato *et al.*, 2011). As such, the fly has proven to be a valuable  
403 model to study heart failure in humans. Here, we presented evidence that the  
404 cardiac phenotypes in COVID-19 might be instigated by SARS-CoV-2 protein  
405 Nsp6. Altogether, expression of Nsp6 increased glycolysis, which led to cardiac  
406 dysfunction in both *Drosophila* and mouse models.

407

408 Our proteomics data revealed that SARS-CoV-2 Nsp6 interacts with host  
409 factors that regulate glycolysis, including the MGA, PCGF6 and TFDP1  
410 transcription factors, which are members (or interactors) of the non-canonical  
411 PRC1.6 complex (Stielow *et al.*, 2018; Llabata *et al.*, 2020). MYC-associated  
412 factor X (MAX) is another member of this complex. This  
413 MGA/PCGF6/TFDP1/MAX (MGA/MAX) complex recognizes and binds the  
414 same sequences as those targeted by MYC/MAX, and thus acts as an  
415 antagonist of MYC/MAX complex-mediated gene expression. MYC/MAX  
416 regulates genes encoding glycolysis pathway proteins, thus inducing  
417 glycolysis activity through increased gene expression. By binding the MGA,  
418 PCGF6 and TFDP1 transcription factors, SARS-CoV-2 Nsp6 inhibits formation  
419 of the MGA/MAX complex, which shifts the balance towards MYC/MAX (Figure  
420 7). Our data show that increased MYC can be directly responsible for increased  
421 glycolysis, *i.e.* Pgi activity and NADH basal levels, in fly hearts.

422

423 Consistent with more active glycolysis, other genes upregulated by SARS-  
424 CoV2 Nsp-6 in the fly heart include those involved in the mitochondrial TCA cycle  
425 and oxidative phosphorylation (OxPhos). OxPhos generates reactive oxygen  
426 species (ROS), which have been associated with several physiological  
427 functions as well as pathology—like the sterile inflammatory response often  
428 observed in heart failure (Zhou and Tian, 2018). Two studies had demonstrated  
429 a role for the HIF1 $\alpha$ -glycolysis axis in SARS-CoV-2 infection, but neither had  
430 specified the viral protein responsible. The first study, showed SARS-CoV-2  
431 induces mitochondrial ROS in monocytes, during later stages in the viral life  
432 cycle (Codo *et al.*, 2020). The second study found increased activity of the  
433 HIF1 $\alpha$ -glycolysis fatty acid synthesis axis in an *in vitro* human airway epithelium  
434 model; that used ciliated-like cells in human pluripotent stem cell-derived airway  
435 organoids, which were permissive to SARS-CoV-2 infection (Duan *et al.*, 2021).  
436 Our findings show dysregulated glycolysis in heart related to SARS-CoV-2;  
437 specifically, we demonstrate the viral Nsp6 protein is responsible, suggesting  
438 this might be the culprit in lung epithelium as well. In fact, we found *sima*,  
439 *Drosophila* ortholog of *HIF-1a*, was significantly upregulated in fly heart  
440 expressing SARS-CoV-2 Nsp6 (RNAseq, 1.47 fold, adj. P = 0.0364). Increased  
441 ROS triggered the hypoxia-inducible factor-1a (HIF-1a)-dependent pathway  
442 which in turn upregulated glycolysis genes (Codo *et al.*, 2020; Duan *et al.*,  
443 2021). This could potentially provide a feedback loop reinforcing the initial  
444 increase in glycolysis activity by Nsp6. During heart failure, cardiomyocytes  
445 switch from fatty acid to glucose metabolism in order to optimize the ATP  
446 production to oxygen consumption ratio (Tran and Wang, 2019). Thus, while  
447 increased glycolysis activity acts as a protective mechanism under cardiac

448 pathogenic conditions, it might only exacerbate the overactive glycolysis during  
449 SARS-CoV-2 infection induced by its Nsp6 protein. Further studies are needed  
450 to delineate these observations.

451

#### 452 **SARS-CoV-2 control of host glycolysis benefits virus replication**

453 SARS-CoV-2 Nsp6 upregulated glycolysis as well as related pathways, such  
454 as TCA and OxPhos in the mitochondria, and the pentose phosphate pathway  
455 (PPP) in the cytosol. In addition to generating bioenergy in the form of ATP,  
456 these processes generate metabolites to support various biological processes,  
457 including biosynthesis and protein modification. For example, glucose-6-P, an  
458 intermediate of glycolysis, also provides the starting metabolite for the PPP.  
459 The PPP mediates *de novo* purine synthesis which is thought to play a role in  
460 virus replication by providing essential metabolites. In fact, a recent publication  
461 showed glucose was depleted in cells (VeroE6) infected with SARS-CoV-2 and  
462 demonstrated the virus hijacks the folate and one carbon metabolic pathways  
463 to favor *de novo* purine synthesis and to support replication early in the viral life  
464 cycle (Zhang *et al.*, 2021). Similarly, our data showed that genes belonging to  
465 'purine metabolic processes' and 'one carbon pool by folate' are significantly  
466 upregulated in *Nsp6* expressing fly hearts. These data show that increased  
467 glycolysis supports SARS-CoV-2 virus replication. Moreover, our findings  
468 suggest SARS-CoV-2 Nsp6 protein mediates this process (Figure 7).

469

#### 470 **Altered glycolysis, in the heart, following SARS-CoV-2 infection**

471 Altered glycolysis following SARS-CoV-2 infection has been reported in human  
472 cells and patients, such as in human Caco-2 cells, which are highly permissive

473 to infection (Bojkova *et al.*, 2020). Host-dependent dysregulation of glycolysis,  
474 among other metabolic pathways, following SARS-CoV-2 infection was also  
475 evident in transcriptomic data obtained from different human respiratory cells  
476 lines and various patient samples (Moolamalla *et al.*, 2021). In addition, single-  
477 nucleus RNA-seq data from lung tissue of deceased COVID-19 patients found  
478 changes in genes related to several metabolic pathways, including glycolysis  
479 and OxPhos (Li *et al.*, 2022). Besides, mild ischemia (early stages) is  
480 characterized by increased glycolytic flux with concomitant increased glucose  
481 uptake (Tran and Wang, 2019).

482

483 An *in vivo* study in hamsters infected with SARS-CoV-2 found increased  
484 expression of ROS-related genes in heart tissue (Yang *et al.*, 2021). Of note,  
485 viral transcripts were detected in the left ventricle and atrium and the right  
486 atrium, but not the right ventricle; this suggests the sampling site might matter.  
487 The same study also found significantly altered ROS in heart samples of  
488 deceased COVID-19 patients compared to samples from non-COVID-19  
489 individuals (Yang *et al.*, 2021). These findings are in line with those we made  
490 in fly. In fact, increased mitochondrial dysfunction and increased ROS are well-  
491 known contributors to cardiac disease (Peoples *et al.*, 2019). Together, the  
492 direct (*in vivo* animal models) and indirect (human *in vitro* and patient non-heart  
493 tissue) data support the notion of SARS-CoV-2 Nsp6 induced glycolysis, and  
494 ROS, in the heart during COVID-19 (model in Figure 7).

495

496 **SARS-CoV-2 presence in the heart of mammalian models and COVID-19**  
497 **patients**

498 The data make a case for SARS-CoV-2 Nsp6-induced dysregulated glycolysis  
499 driving cardiac pathology. However, the cardiac injury, and ultimately heart  
500 failure, in COVID-19 could be a secondary effect stemming from the increased  
501 thrombotic activity or cytokine storm associated cardiomyopathy, rather than a  
502 primary effect directly caused by virus infection. Virus in cardiac tissue has been  
503 reported in *in vivo* mammalian models. In (6/9) hamsters intranasally infected  
504 with SARS-CoV-2, cardiomyocytes were found damaged, and SARS-CoV-2  
505 was detected within the cells (Yang *et al.*, 2021). Mice, unlike hamsters, are not  
506 naturally susceptible to SARS-CoV-2 infection. However, transgenic mice that  
507 express HFH4-hACE2—the human ACE2 receptor that facilitates virus entry—  
508 showed cardiac pathology following SARS-CoV-2 infection, and low viral RNA  
509 copies were detected in the hearts of some of the mice (Jiang *et al.*, 2020).  
510 Findings in human patients have repeatedly shown virus present in cardiac  
511 tissue; on the other hand, virus entry of cardiomyocytes specifically remains a  
512 matter of debate. One early study reported no evidence for relevant viral  
513 presence (the meaning of “relevant” was not defined) in cardiac tissue in 40  
514 deceased patients diagnosed with severe SARS-CoV-2 infection during the first  
515 wave of the pandemic (Dal Ferro *et al.*, 2021). However, findings that support  
516 viral entry into cardiac tissue have been steadily accumulating. Early studies  
517 detected SARS-CoV-2 genomes in endomyocardial biopsies of patients with  
518 cardiac injury (Escher *et al.*, 2020; Tavazzi *et al.*, 2020). In addition, multiple  
519 autopsy studies have reported direct evidence of SARS-CoV-2 presence in  
520 heart tissue in those infected with the virus [16/39 (41.0%) deceased patients  
521 positive for SARS-CoV-2 infection (Lindner *et al.*, 2020); 8/8 deceased patients  
522 with COVID-19 diagnosis and morphological signs of myocarditis (Kogan *et al.*,

523 2022), including histopathology to show SARS-CoV-2 present in the  
524 cardiomyocytes]. A large study reported 49/97 (48%) autopsies with SARS-  
525 CoV-2 RNA in the cardiomyocytes (D'Onofrio *et al.*, 2021) and case reports  
526 similarly found SARS-CoV-2 present in cardiomyocytes for heart tissue  
527 obtained from deceased COVID-19 patients [six patients (Bulfamante *et al.*,  
528 2020); one patient (Gauchotte *et al.*, 2021; Nakamura *et al.*, 2021)]. However,  
529 while one of the larger studies did detect relevant SARS-CoV-2 virus load in  
530 heart tissue in 41/95 deceased (43%; RNA sequencing), it was co-localized  
531 with wheat germ agglutinin (WGA) suggesting the virus was present in  
532 interstitial cells surrounding the large cardiomyocytes. Only rarely did they  
533 detect viral RNA within the cardiomyocytes (Bräuninger *et al.*, 2022). Therefore,  
534 while other pathomechanisms, such as hypoxemia caused by respiratory  
535 failure, (hyper)inflammation, or macrophages originating in the lungs,  
536 undoubtedly contribute to cardiac distress. Together, the findings support direct  
537 action of SARS-CoV-2 in cardiac tissue, and within cardiomyocytes, as a cause  
538 of the cardiac pathology observed in COVID-19 patients.

539

#### 540 **Inhibition of glycolysis as a treatment strategy for COVID-19**

541 Our findings are in line with several human cell culture studies that showed  
542 increased glycolysis following infection with SARS-CoV-2. In human Caco-2  
543 cells, SARS-CoV-2 infection affected the carbon metabolism (Bojkova *et al.*,  
544 2020). Treating the cells with 2DG, a potent inhibitor of the glycolysis pathway,  
545 prevented virus replication *in vitro*, and induced changes in an endoplasmic  
546 reticulum (ER) protein known to regulate lipid metabolism (Bojkova *et al.*, 2020).  
547 In human pluripotent stem cell-derived airway organoids, the small molecule

548 GW6271 (FDA-approved) both blocked SARS-CoV-2 infection and virus  
549 replication; GW6271 acts by inhibiting the HIF1 $\alpha$ -glycolysis axis (Duan *et al.*,  
550 2021). A study in Vero E6 cells found that 2DG treatment reduced SARS-CoV-  
551 2-induced glycolysis activity, attenuated cytopathy, and reduced viral  
552 replication (Bhatt *et al.*, 2022). A recent study in healthy control mice showed  
553 that 2DG treatment-induced metabolic changes in the mouse heart would  
554 oppose those previously observed in SARS-CoV-2 infected cells (Aiestaran-  
555 Zelaia *et al.*, 2022); thus, providing indirect support for 2DG in treating SARS-  
556 CoV-2-associated cardiac disease. Our findings expand on these previous  
557 studies by providing *in vivo* data (fly and mouse) that demonstrate SARS-CoV-  
558 2 Nsp6 protein can cause cardiac phenotype, this phenotype is marked by  
559 increased glycolysis activity—due to interaction of Nsp6 with a host protein  
560 complex that regulates glycolysis—and dysfunctional mitochondria, and this  
561 cardiac phenotype can be effectively treated with 2DG.

562

563 Regards 2DG treatment for COVID-19 in humans, a combination therapy of  
564 2DG and low dose radiation has been proposed to treat the COVID-19-  
565 associated cytokine storm (Verma *et al.*, 2020). In India, 2DG treatment has  
566 received emergency use approval to curb a devastating recent COVID-19  
567 outbreak (Halder and Mehta, 2021); a clinical trial in India to investigate the  
568 effectivity of 2DG to treat COVID-19 has been registered with WHO  
569 (registration: CTRI/2021/01/030231). Moreover, WP1122, a 2DG derivative is  
570 pursued as a lead compound against COVID-19 by targeting glycolysis to inhibit  
571 virus replication (Moleculin Biotech, TX, USA). One of the main hurdles to start  
572 clinical trials is the requirement for supporting data from animal models. The

573 outcomes of this trial will be a major first step to establish the potential of 2DG  
574 as a COVID-19 therapeutic.

575

576 Of note, another strategy to inhibit glycolysis is to lower the available glucose  
577 levels by a ketogenic diet. A study in mice (mCoV-A59 driven infection) showed  
578 protection induced by the ketogenic immunometabolic switch (Ryu *et al.*, 2021),  
579 and preliminary findings from an early clinical trial showed reduced severity  
580 (based on need on use of intensive care unit and death) in COVID-19 patients  
581 on a ketogenic diet compared to those on a eucaloric standard diet (Sukkar and  
582 Bassetti, 2020; Sukkar *et al.*, 2021). These are preliminary results, and mostly  
583 focused on immunological measures; however, additional clinical trials are  
584 under way (<https://clinicaltrials.gov>) and will hopefully shed light on the effect of  
585 a ketogenic diet on the COVID-19-associated cardiac pathological outcomes.

586

587 Taken together, our findings demonstrate virus control of host glycolysis and  
588 related pathways in the heart (fly and mouse)—likely to benefit virus  
589 replication—that this pathology is mediated by SARS-CoV-2 Nsp6 protein, and  
590 that treatment with 2DG provides a promising therapeutic strategy for  
591 cardiovascular pathology in COVID-19.

592

593

## 594 **MATERIALS AND METHODS**

595

### 596 **Fly strains**

597 All *Drosophila* fly stocks were reared and kept on standard food at 25°C.

598 *4XHand-Gal4/CyO* ['Curly O' (CyO) balancer chromosome with curly wing  
599 phenotype] and UAS-*SARS-CoV-2* transgenic flies were generated previously  
600 (Zhu *et al.*, 2021). The other fly lines were obtained from the Bloomington  
601 *Drosophila* Stock Center (Indiana University, IN): *w*<sup>1118</sup> (#BL-3605), UAS-*Pgi*-  
602 OE (#BL-60676), and UAS-*Myc*-OE (#BL-9674, and #BL-64759).

603

#### 604 **Mortality at eclosion**

605 To assay the effect of viral gene expression on fly viability, a balancer system  
606 was used. *Drosophila* lines that overexpressed (OE) a UAS-*SARS-CoV-2* gene  
607 were crossed with the *4XHand-Gal4/CyO* line. Offspring either carried UAS-  
608 *SARS-CoV-2* gene-OE/*CyO* in which the balancer chromosome resulted in a  
609 *CyO* curly wing phenotype without transgene expression, or they carried UAS-  
610 *SARS-CoV-2* gene-OE/*4XHand-Gal4* resulting in transgenic lines with straight  
611 wings that express the *SARS-CoV-2* gene driven by *4XHand-Gal4* for heart-  
612 specific expression. Embryo progenies were collected and allowed to develop  
613 under standard conditions. Mortality at eclosion (adult emergence from pupa  
614 stage) was based on the percentage of flies with *SARS-CoV-2* gene expression  
615 (straight wing) that failed to emerge as adults, relative to siblings that did not  
616 express the *SARS-CoV-2* gene construct (*CyO* wing). Results are presented  
617 as a Mortality Index calculated by: (*CyO* wing – straight wing) / *CyO* wing × 100.

618

#### 619 **Adult survival assay**

620 Following egg-laying, *Drosophila* larvae were kept at 25°C, standard conditions  
621 and an optimal temperature for UAS-*transgene* expression. Adult male flies  
622 were maintained in vials in groups of 20 or fewer. The number of living flies in

623 each group was recorded every second day. The assay was carried out until  
624 no survivors were left for any of the fly lines. Per genotype 100 flies were  
625 assayed.

626

### 627 ***Drosophila* heart imaging**

628 Adult flies were dissected and fixed for 10 min in 4% paraformaldehyde in  
629 phosphate-buffered saline (1×PBS). Flies were incubated in block solution  
630 containing 0.1% Triton X-100 plus 2% bovine serum albumin (BSA) in 1×PBS  
631 for 40 min, then incubated with either Alexa Fluor R647 phalloidin (Thermo  
632 Fisher; 1:1,000 in block solution) by itself or combined with primary antibody  
633 ATP5a (Abcam, ab14748; 1:1,000 in block solution) overnight at 4°C. Next day,  
634 the flies were washed three times with 1×PBS, then imaged or for  
635 immunostaining incubated with secondary Alexa Fluor 488 goat anti-mouse  
636 antibody (Thermo Fisher; 1:1,000 in block solution) for 2 hrs at room  
637 temperature, and then washed three times with 1×PBS. Confocal imaging was  
638 performed using a ZEISS LSM 900 with Airyscan 2 and a 63× Plan-Apochromat  
639 1.4 N.A. oil objective (ZEN image acquisition software). For quantitative  
640 comparisons of fluorescence intensity, common settings were chosen to avoid  
641 oversaturation. ImageJ software (version 1.49) was used to process the  
642 images. For quantitative comparisons of cardiac muscle fiber density, we  
643 analyzed six control flies and six RNAi expressing flies of each genotype.

644

### 645 **Optical coherence tomography (OCT) measurements and analysis of** 646 **cardiac function**

647 Cardiac function in adult *Drosophila* was measured using an optical coherence

648 tomography (OCT) system (Bioptigen Inc.). For this, 4-day-old flies were  
649 anesthetized by carbon dioxide (CO<sub>2</sub>) for 3–5 minutes and females were  
650 preselected from each group. Each fly was gently placed on a plate with  
651 petroleum jelly (Vaseline) for immobilization with the dorsal aspect facing the  
652 OCT microscopy source, then rested for at least 10 minutes to ensure the fly  
653 was fully awake. For each genotype, 10 control and 10 RNAi expressing flies  
654 were used. OCT was used to record the adult heart rhythm and heart wall  
655 movement at the same position, *i.e.* the cardiac chamber in the abdominal  
656 segments A2 of each fly. M-mode images recorded the heart wall movement  
657 during the cardiac cycle. ImageJ software (version 1.49) (Schneider, Rasband  
658 and Eliceiri, 2012) was used to process the images. The diastolic dimension  
659 and systolic diameter were processed, measured, and determined based on  
660 three consecutive heart beats. The heart rate was determined by counting the  
661 total number of beats that occurred during a 2-second recording.

662

### 663 **RNA extraction and sequencing of *Drosophila* heart cells**

664 For each sample, hearts from fifty-one—week-old adult flies were manually  
665 dissected and collected directly into ice-cold TRIzol LS reagent (Thermo Fisher  
666 Scientific). Then, RNA extraction was performed according to the instructions  
667 provided by the manufacturer (Direct-zol RNA Microprep, Zymo Research).  
668 RNA quality and concentration were analyzed by agarose gel electrophoresis,  
669 NanoDrop 8000 Spectrophotometer, and Agilent 2100. More than 400 ng total  
670 RNA for each sample was used in subsequent library preparation and  
671 sequencing.

672

673 Illumina-based RNAseq library preparation and subsequent paired-end  
674 sequencing were performed by Novogene (Beijing, China). Novogene also  
675 carried out mapping of the short-reads, their quantification, and initial differential  
676 analyses. In brief, reads that contained Illumina-adaptor sequences or those  
677 considered to be of poor quality (> 10% uncertain base nucleotides, or Phred  
678 score < 5 for over 50% of the reads) were removed before mapping. The short-  
679 reads, generated from the RNAseq, were mapped to the Berkeley Drosophila  
680 Genome Project (BDGP) reference genome release 6 (BDGP 6) using HISAT2  
681 version 2.0.5 (Kim *et al.*, 2019) using parameters: --dta --phred33. For gene-  
682 level quantification, the *Drosophila* gene annotation model from Ensembl  
683 version 100 (Yates *et al.*, 2020), which corresponds to Flybase 6.28 (Larkin *et*  
684 *al.*, 2021), was used with featureCounts version 1.5.0-p3 (with default  
685 parameters). DESeq2 version 1.2.0 was used for differential expression  
686 analysis (Love, Huber and Anders, 2014).

687

688 ClusterProfiler version 3.18.1 (Yu *et al.*, 2012) was used for the Gene Ontology  
689 (GO) and KEGG pathway analyses. Classification of glycolysis, pentose  
690 phosphate pathway (PPP), citric acid (a.k.a. TCA) cycle, and oxidative  
691 phosphorylation (OxPhos) were based on KEGG database annotations  
692 (Kanehisa *et al.*, 2016). The gene conservation scores (fly-human) were  
693 obtained from the DRSC Integrative Ortholog Prediction Tool (DIOPT) version  
694 8 (Hu *et al.*, 2011).

695

#### 696 **Pgi activity and NADH level measurement**

697 The enzymatic activity of Phosphoglucose isomerase (Pgi) and NADH levels

698 were determined using the Phosphoglucose Isomerase Colorimetric Assay Kit  
699 (Sigma) according to manufacturer's protocol. For each sample, one fly was  
700 homogenized and diluted 1:50. Six samples were measured for each genotype.  
701 The colorimetric reaction was measured at 450 nm on a Spark multimode  
702 microplate reader (Tecan, Switzerland; SparkControl software, v2.3).

703

#### 704 **Mass spectrometry in HEK 293T cells**

705 Cell culture, sample preparation, mass spectrometry and data analysis were  
706 carried out as described before (Lee *et al.*, 2021). In brief, HEK 293T cells  
707 (human embryonic kidney-derived 293T cell line) were cultured and maintained  
708 in DMEM medium (Corning cellgro) containing 10% fetal bovine serum and  
709 Penicillin-Streptomycin (10 units/ml). The SARS-CoV-2 *Nsp6* cDNA fragment  
710 was codon-optimized and assembled into the pCMV6 vector for C-terminal  
711 tagging with mCherry (mCh)-FLAG. The FLAG-tag was used for affinity  
712 purification using FLAG agarose beads (Sigma). The proteins thus pulled down  
713 were solubilized in 5% sodium deoxycholate, then washed, reduced, alkylated,  
714 and trypsinized on the filter (Wiśniewski *et al.*, 2009; Erde, Loo and Loo, 2014).  
715 Tryptic peptides were separated on a nanoACQUITY UPLC analytical column  
716 (BEH130 C18, Waters) over a 165 min linear acetonitrile gradient (3–40%) with  
717 0.1% formic acid on a Waters nano-ACQUITY UPLC system and analyzed on  
718 a coupled Thermo Scientific Orbitrap Fusion Lumos Tribrid mass spectrometer  
719 (Williamson *et al.*, 2016). Label-free quantification was performed using Minora,  
720 an aligned AMRT (Accurate Mass and Retention Time) cluster quantification  
721 algorithm (Thermo Scientific, 2017) using extracted ion chromatograms.  
722 Protein abundance was measured by Hi3 method (Silva *et al.*, 2006).

723 Quantitation between samples was normalized by mCh abundance.

724

725 Based on a previous study (Lambert *et al.*, 2018) we identified the transcription  
726 factors present among the human proteins that bind SARS-CoV-2 Nsp6 in our  
727 mass spec results. Physical interactions among these transcription factors, as  
728 well as MYC and MAX, were determined and visualized using the STRING  
729 database version 11 (Szklarczyk *et al.*, 2019).

730

### 731 **Treatment with 2-deoxy-D-glucose**

732 Compound 2-deoxy-D-glucose (2DG) (SIGMA, SIG-D8375) was dissolved in  
733 water and added to standard fly food at various concentrations (2, 10 or 50 mM  
734 2DG dilution). For controls, water alone (0 mM) was added to the fly food. Flies  
735 were treated from the 1<sup>st</sup> instar larval stage.

736

### 737 **Mice**

738 The procedures for animal use were approved by the University of Maryland  
739 School of Medicine Institutional Animal Care and Use Committee (ACUC). Wild-  
740 type C57BL/6J mice were purchased from the Jackson Laboratory (Bar Harbor,  
741 ME). Male and female mice were paired and observed for pregnancy by the  
742 presence of the vaginal plug (E0.5). At E12.5, pregnant female mice were  
743 euthanized, and embryos were collected for primary cardiomyocyte isolation.

744

### 745 **Primary cardiomyocyte isolation and culture**

746 Mice embryonic primary cardiomyocytes were isolated using the Pierce Primary  
747 Cardiomyocyte Isolation Kit (Thermo Fisher Scientific). At E12.5 mice were

748 sacrificed to collect embryonic hearts. Briefly, E12.5 heart were collected  
749 individually and washed three times with 1×PBS and Hank's Balanced Salt  
750 Solution (HBSS). Washed hearts were treated with lysis buffer and incubated  
751 at 37°C with 5% CO<sub>2</sub> for 30 min. Lysis buffer was removed and the cells were  
752 washed with ice-cold HBSS, twice. Then, prewarmed cardiomyocyte culture  
753 medium was added to each heart cell lysate and suspended by gently braking  
754 up the cells with a pipette. Finally, the mouse primary cardiomyocytes were  
755 seeded in a Matrigel-coated 6-well culture plate at 1x10<sup>6</sup> cells/well density and  
756 cultured at 37°C with 5% CO<sub>2</sub>. After 48 hrs in culture, the cardiomyocytes were  
757 transfected (using Lipofectamine 2000 transfection reagent; Invitrogen) with  
758 either control pcDNA3 plasmid (Lipo; control) or SARS-CoV-2 *Nsp6* plasmid,  
759 and then incubated overnight. The next day, culture medium was replaced with  
760 fresh medium and the cells were incubated for 48 hrs with or without 2DG  
761 treatment (1mM). Following, the cells were collected for further morphological  
762 and molecular analysis.

763

#### 764 **RNA extraction, reverse transcription and RT-PCR**

765 Mouse primary cardiomyocyte RNA was extracted using the RNeasy Mini Kit  
766 (Qiagen) and reverse transcribed using q-script cDNA Supermix (QuantaBio  
767 Biosciences) following manufacturer's guidelines and protocol. RNA samples  
768 were analyzed for quality and concentration using a NanoDrop ND-1000  
769 Spectrophotometer. Next, expression of the following genes was analyzed in  
770 mice E12.5 primary cardiomyocytes: *ANP*, *BNP*, *Gpi1*, *Pfkm*, *Pgam2*, and *Eno1*  
771 with GAPDH as an endogenous reference gene (Supplemental Table S3). The  
772 lipofectamine treated cells served as control to the cardiomyocytes transfected

773 with SARS-CoV-2 *Nsp6*. The RT-PCR was performed on Step One Plus  
774 System (Applied Biosystem, Grand Island, NY), using the SsoFast EvaGreen  
775 Supermix (Bio-Rad) with a total of 20  $\mu$ l reaction volume: 2  $\mu$ l cDNA, 4  $\mu$ l  
776 SsoFast EvaGreen Supermix, 2  $\mu$ l F/R primer mix, and 12  $\mu$ l water, followed by  
777 standard touchdown PCR protocol.

778

### 779 **Primary cardiomyocyte contraction and Ca<sup>2+</sup> wave analyses**

780 The contraction rate (beating) and Ca<sup>2+</sup> absorption waves of the mouse primary  
781 cardiomyocytes were analyzed through confocal microscope using a ZEISS  
782 LSM 900 with Airyscan 2 and a 63 $\times$  Plan-Apochromat 1.4 N.A. oil objective  
783 (ZEN image acquisition software). Contractions of the cardiomyocytes were  
784 manually counted for the number of “beats” in 15 seconds.

785

### 786 **Statistical analysis**

787 Statistical analysis was performed using PAST software (Natural History  
788 Museum, Norway). Mean values are presented along with their standard  
789 deviation (SD). The Student’s t-test was used for comparisons between two  
790 groups. The Kruskal-Wallis H-test followed by a Dunn’s test was used for  
791 comparisons between multiple groups. Statistical significance was defined as  
792  $P < 0.05$ .

793

794

### 795 **ACKNOWLEDGMENTS**

796

797 We thank Dr. Na-Young Rho for providing the cell cultures used for Ca<sup>2+</sup>

798 imaging. We thank the Bloomington *Drosophila* Stock Center at Indiana  
799 University Bloomington (IN) for the *Drosophila* lines.

800

801

## 802 **COMPETING INTERESTS**

803

804 The authors have nothing to declare.

805

806

## 807 **FUNDING**

808

809 This work was supported, in part, by the University of Maryland Baltimore  
810 Institute for Clinical and Translational Research (UMB ICTR) COVID-19  
811 Accelerated Translational Incubator Pilot (ATIP) grant to ZH, and the University  
812 of Maryland School of Pharmacy Mass Spectrometry Center (SOP1841-  
813 IQB2014).

814

815

## 816 **AVAILABILITY OF DATA AND MATERIALS**

817

818 The datasets generated and analyzed during this study have been deposited  
819 at public servers. The RNAseq data can be accessed through the NCBI Gene  
820 Expression Omnibus (GEO) with the following accession number: GSE173835.

821 The mass spectrometry data are available through the Department of  
822 Pharmaceutical Sciences, University of Maryland School of Pharmacy at the

823 UMB-SOP-MetalloCloud repository with the following link:  
824 <https://bit.ly/31XL2Sx>. Any additional data and materials generated during this  
825 study are available upon reasonable request.

826

827

## 828 **AUTHOR CONTRIBUTIONS**

829

830 ZH and JZ designed the study; JZ, GW, XH, HL, WH, PY and JL carried out the  
831 experiments; JZ, GW, XH, HL, JL, JvdL, MAK, PY and ZH analyzed and  
832 interpreted the data; JZ, XH, HL and JL prepared the figures; JvdL and ZH  
833 drafted and edited the manuscript. All authors read and approved the final  
834 version of this manuscript for publication.

835

836

## 837 **REFERENCES**

838 Aiestaran-Zelaia, I. *et al.* (2022) “2 deoxy-D-glucose augments the  
839 mitochondrial respiratory chain in heart,” *Scientific reports*, 12(1), p. 6890.

840 Bader, F. *et al.* (2021) “Heart failure and COVID-19,” *Heart failure reviews*.  
841 Springer Science and Business Media LLC, 26(1), pp. 1–10.

842 Belyaeva, A. *et al.* (2021) “Causal network models of SARS-CoV-2 expression  
843 and aging to identify candidates for drug repurposing,” *Nature communications*,  
844 12(1), p. 1024.

845 Bhatt, A. N. *et al.* (2022) “Glycolytic inhibitor 2-deoxy-d-glucose attenuates  
846 SARS-CoV-2 multiplication in host cells and weakens the infective potential of  
847 progeny virions,” *Life sciences*, 295, p. 120411.

848 Bielecka-Dabrowa, A. *et al.* (2021) “Cardiac manifestations of COVID-19,”  
849 *Reviews in cardiovascular medicine*, 22(2), pp. 365–371.

850 Bojkova, D. *et al.* (2020) “Proteomics of SARS-CoV-2-infected host cells  
851 reveals therapy targets,” *Nature*, 583(7816), pp. 469–472.

852 Bräuninger, H. *et al.* (2022) “Cardiac SARS-CoV-2 infection is associated with  
853 pro-inflammatory transcriptomic alterations within the heart,” *Cardiovascular*

854 *research*, 118(2), pp. 542–555.

855 Bulfamante, G. P. *et al.* (2020) “Evidence of SARS-CoV-2 Transcriptional  
856 Activity in Cardiomyocytes of COVID-19 Patients without Clinical Signs of  
857 Cardiac Involvement,” *Biomedicines*, 8(12). doi:  
858 10.3390/biomedicines8120626.

859 Cammarato, A. *et al.* (2011) “A mighty small heart: the cardiac proteome of  
860 adult *Drosophila melanogaster*,” *PloS one*, 6(4), p. e18497.

861 Chan, C.-M. *et al.* (2007) “The SARS-Coronavirus Membrane protein induces  
862 apoptosis through modulating the Akt survival pathway,” *Archives of*  
863 *Biochemistry and Biophysics*, pp. 197–207. doi: 10.1016/j.abb.2007.01.012.

864 Codo, A. C. *et al.* (2020) “Elevated Glucose Levels Favor SARS-CoV-2  
865 Infection and Monocyte Response through a HIF-1 $\alpha$ /Glycolysis-Dependent  
866 Axis,” *Cell metabolism*, 32(3), pp. 498–499.

867 Dal Ferro, M. *et al.* (2021) “SARS-CoV-2, myocardial injury and inflammation:  
868 insights from a large clinical and autopsy study,” *Clinical research in cardiology:*  
869 *official journal of the German Cardiac Society*, 110(11), pp. 1822–1831.

870 Diop, S. B. and Bodmer, R. (2015) “Gaining Insights into Diabetic  
871 Cardiomyopathy from *Drosophila*,” *Trends in endocrinology and metabolism:*  
872 *TEM*, 26(11), pp. 618–627.

873 D’Onofrio, N. *et al.* (2021) “Glycated ACE2 receptor in diabetes: open door for  
874 SARS-COV-2 entry in cardiomyocyte,” *Cardiovascular diabetology*, 20(1), p.  
875 99.

876 Drucker, D. J. (2021) “Diabetes, obesity, metabolism, and SARS-CoV-2  
877 infection: the end of the beginning,” *Cell metabolism*, 33(3), pp. 479–498.

878 Duan, X. *et al.* (2021) “An airway organoid-based screen identifies a role for the  
879 HIF1 $\alpha$ -glycolysis axis in SARS-CoV-2 infection,” *Cell reports*, 37(6), p. 109920.

880 Dweck, M. R. *et al.* (2020) “Global evaluation of echocardiography in patients  
881 with COVID-19,” *European heart journal cardiovascular Imaging*, 21(9), pp.  
882 949–958.

883 Erde, J., Loo, R. R. O. and Loo, J. A. (2014) “Enhanced FASP (eFASP) to  
884 increase proteome coverage and sample recovery for quantitative proteomic  
885 experiments,” *Journal of proteome research*, 13(4), pp. 1885–1895.

886 Escher, F. *et al.* (2020) “Detection of viral SARS-CoV-2 genomes and  
887 histopathological changes in endomyocardial biopsies,” *ESC heart failure*, 7(5),  
888 pp. 2440–2447.

889 Gauchotte, G. *et al.* (2021) “SARS-Cov-2 fulminant myocarditis: an autopsy and  
890 histopathological case study,” *International journal of legal medicine*, 135(2),  
891 pp. 577–581.

892 Gaziano, L. *et al.* (2021) “Actionable druggable genome-wide Mendelian

893 randomization identifies repurposing opportunities for COVID-19,” *Nature*  
894 *medicine*, 27(4), pp. 668–676.

895 Gordon, D. E., Jang, G. M., *et al.* (2020) “A SARS-CoV-2 protein interaction  
896 map reveals targets for drug repurposing,” *Nature*, 583(7816), pp. 459–468.

897 Gordon, D. E., Hiatt, J., *et al.* (2020) “Comparative host-coronavirus protein  
898 interaction networks reveal pan-viral disease mechanisms,” *Science*,  
899 370(6521). doi: 10.1126/science.abe9403.

900 Guo, T. *et al.* (2020) “Cardiovascular Implications of Fatal Outcomes of Patients  
901 With Coronavirus Disease 2019 (COVID-19),” *JAMA cardiology*, 5(7), pp. 811–  
902 818.

903 Guzzi, P. H. *et al.* (2020) “Master Regulator Analysis of the SARS-CoV-  
904 2/Human Interactome,” *Journal of clinical medicine research*, 9(4). doi:  
905 10.3390/jcm9040982.

906 Halder, S. and Mehta, A. K. (2021) “2-Deoxy-D-glucose: is this the final cure for  
907 COVID-19: or yet another mirage?,” *European review for medical and*  
908 *pharmacological sciences*, 25(13), pp. 4448–4450.

909 Harnish, J. M., Link, N. and Yamamoto, S. (2021) “Drosophila as a Model for  
910 Infectious Diseases,” *International journal of molecular sciences*, 22(5). doi:  
911 10.3390/ijms22052724.

912 Ho, G. *et al.* (2021) “Diabetes, inflammation, and the adiponectin paradox:  
913 Therapeutic targets in SARS-CoV-2,” *Drug discovery today*. doi:  
914 10.1016/j.drudis.2021.03.013.

915 Hu, Y. *et al.* (2011) “An integrative approach to ortholog prediction for disease-  
916 focused and other functional studies,” *BMC bioinformatics*, 12, p. 357.

917 Hughes, T. T. *et al.* (2012) “Drosophila as a genetic model for studying  
918 pathogenic human viruses,” *Virology*, 423(1), pp. 1–5.

919 Hussain, M. *et al.* (2020) “Dataset for homologous proteins in Drosophila  
920 melanogaster for SARS-CoV-2/human interactome,” *Data in brief*, 32, p.  
921 106082.

922 Jiang, R.-D. *et al.* (2020) “Pathogenesis of SARS-CoV-2 in Transgenic Mice  
923 Expressing Human Angiotensin-Converting Enzyme 2,” *Cell*, 182(1), pp. 50-  
924 58.e8.

925 Kanehisa, M. *et al.* (2016) “KEGG as a reference resource for gene and protein  
926 annotation,” *Nucleic acids research*, 44(D1), pp. D457-62.

927 Kanehisa, M. *et al.* (2021) “KEGG: integrating viruses and cellular organisms,”  
928 *Nucleic acids research*, 49(D1), pp. D545–D551.

929 Kim, D. *et al.* (2019) “Graph-based genome alignment and genotyping with  
930 HISAT2 and HISAT-genotype,” *Nature biotechnology*, 37(8), pp. 907–915.

931 Kogan, E. *et al.* (2022) “Morphologically, immunohistochemically and PCR

932 proven lymphocytic viral peri-, endo-, myocarditis in patients with fatal COVID-  
933 19,” *Diagnostic pathology*, 17(1), p. 31.

934 Lambert, S. A. *et al.* (2018) “The Human Transcription Factors,” *Cell*, 172(4),  
935 pp. 650–665.

936 Larkin, A. *et al.* (2021) “FlyBase: updates to the *Drosophila melanogaster*  
937 knowledge base,” *Nucleic acids research*, 49(D1), pp. D899–D907.

938 Lee, J.-G. *et al.* (2021) “Characterization of SARS-CoV-2 proteins reveals Orf6  
939 pathogenicity, subcellular localization, host interactions and attenuation by  
940 Selinexor,” *Cell & Bioscience*. doi: 10.1186/s13578-021-00568-7.

941 van de Leemput, J. and Han, Z. (2021a) “*Drosophila*, a powerful model to study  
942 virus-host interactions and pathogenicity in the fight against SARS-CoV-2,” *Cell*  
943 *& bioscience*. Springer Science and Business Media LLC, 11(1), p. 110.

944 van de Leemput, J. and Han, Z. (2021b) “Understanding Individual SARS-CoV-  
945 2 Proteins for Targeted Drug Development against COVID-19,” *Molecular and*  
946 *cellular biology*, 41(9), p. e0018521.

947 Li, J. *et al.* (2021) “Virus-Host Interactome and Proteomic Survey Reveal  
948 Potential Virulence Factors Influencing SARS-CoV-2 Pathogenesis,” *Med*, pp.  
949 99-112.e7. doi: 10.1016/j.medj.2020.07.002.

950 Li, S. *et al.* (2022) “Cellular metabolic basis of altered immunity in the lungs of  
951 patients with COVID-19,” *Medical microbiology and immunology*, 211(1), pp.  
952 49–69.

953 Lindner, D. *et al.* (2020) “Association of Cardiac Infection With SARS-CoV-2 in  
954 Confirmed COVID-19 Autopsy Cases,” *JAMA cardiology*, 5(11), pp. 1281–  
955 1285.

956 Llabata, P. *et al.* (2020) “Multi-Omics Analysis Identifies MGA as a Negative  
957 Regulator of the MYC Pathway in Lung Adenocarcinoma,” *Molecular cancer*  
958 *research: MCR*, 18(4), pp. 574–584.

959 Love, M. I., Huber, W. and Anders, S. (2014) “Moderated estimation of fold  
960 change and dispersion for RNA-seq data with DESeq2,” *Genome biology*,  
961 15(12), p. 550.

962 Moolamalla, S. T. R. *et al.* (2021) “Host metabolic reprogramming in response  
963 to SARS-CoV-2 infection: A systems biology approach,” *Microbial*  
964 *pathogenesis*, 158, p. 105114.

965 Moustaqil, M. *et al.* (2021) “SARS-CoV-2 proteases PLpro and 3CLpro cleave  
966 IRF3 and critical modulators of inflammatory pathways (NLRP12 and TAB1):  
967 implications for disease presentation across species,” *Emerging microbes &*  
968 *infections*. Informa UK Limited, 10(1), pp. 178–195.

969 Nakamura, Y. *et al.* (2021) “SARS-CoV-2 is localized in cardiomyocytes: a  
970 postmortem biopsy case,” *International journal of infectious diseases: IJID:*  
971 *official publication of the International Society for Infectious Diseases*, 111, pp.

972 43–46.

973 Pajak, B. *et al.* (2019) “2-deoxy-d-glucose and its analogs: From diagnostic to  
974 therapeutic agents,” *International journal of molecular sciences*. MDPI AG,  
975 21(1), p. 234.

976 Parkinson, N. *et al.* (2020) “Dynamic data-driven meta-analysis for prioritisation  
977 of host genes implicated in COVID-19,” *Scientific reports*, 10(1), p. 22303.

978 Peoples, J. N. *et al.* (2019) “Mitochondrial dysfunction and oxidative stress in  
979 heart disease,” *Experimental & molecular medicine*, 51(12), pp. 1–13.

980 Perham, R. N. (1990) “The fructose-1,6-bisphosphate aldolases: same  
981 reaction, different enzymes,” *Biochemical Society transactions*, 18(2), pp. 185–  
982 187.

983 Puntmann, V. O. *et al.* (2020) “Outcomes of Cardiovascular Magnetic  
984 Resonance Imaging in Patients Recently Recovered From Coronavirus  
985 Disease 2019 (COVID-19),” *JAMA cardiology*, 5(11), pp. 1265–1273.

986 Rajpal, S. *et al.* (2021) “Cardiovascular Magnetic Resonance Findings in  
987 Competitive Athletes Recovering From COVID-19 Infection,” *JAMA cardiology*,  
988 6(1), pp. 116–118.

989 Ryu, S. *et al.* (2021) “Ketogenic diet restrains aging-induced exacerbation of  
990 coronavirus infection in mice,” *eLife*, 10. doi: 10.7554/eLife.66522.

991 Schneider, C. A., Rasband, W. S. and Eliceiri, K. W. (2012) “NIH Image to  
992 ImageJ: 25 years of image analysis,” *Nature methods*, 9(7), pp. 671–675.

993 Sellick, C. A., Campbell, R. N. and Reece, R. J. (2008) “Galactose metabolism  
994 in yeast-structure and regulation of the leloir pathway enzymes and the genes  
995 encoding them,” *International review of cell and molecular biology*, 269, pp.  
996 111–150.

997 Shi, S. *et al.* (2020) “Association of Cardiac Injury With Mortality in Hospitalized  
998 Patients With COVID-19 in Wuhan, China,” *JAMA cardiology*, 5(7), pp. 802–  
999 810.

1000 Shin, D. *et al.* (2020) “Papain-like protease regulates SARS-CoV-2 viral spread  
1001 and innate immunity,” *Nature*, 587(7835), pp. 657–662.

1002 Silva, J. C. *et al.* (2006) “Absolute quantification of proteins by LCMSE: a virtue  
1003 of parallel MS acquisition,” *Molecular & cellular proteomics: MCP*, 5(1), pp.  
1004 144–156.

1005 Singh, A. and Irvine, K. D. (2012) “Drosophila as a model for understanding  
1006 development and disease,” *Developmental dynamics: an official publication of  
1007 the American Association of Anatomists*, 241(1), pp. 1–2.

1008 Sottnik, J. L. *et al.* (2011) “Glycolysis inhibition by 2-deoxy-D-glucose reverts  
1009 the metastatic phenotype in vitro and in vivo,” *Clinical & experimental  
1010 metastasis*, 28(8), pp. 865–875.

- 1011 Stielow, B. *et al.* (2018) “MGA, L3MBTL2 and E2F6 determine genomic binding  
1012 of the non-canonical Polycomb repressive complex PRC1.6,” *PLoS genetics*,  
1013 14(1), p. e1007193.
- 1014 Sukkar, S. G. *et al.* (2021) “Clinical efficacy of eucaloric ketogenic nutrition in  
1015 the COVID-19 cytokine storm: A retrospective analysis of mortality and  
1016 intensive care unit admission,” *Nutrition* , 89, p. 111236.
- 1017 Sukkar, S. G. and Bassetti, M. (2020) “Induction of ketosis as a potential  
1018 therapeutic option to limit hyperglycemia and prevent cytokine storm in COVID-  
1019 19,” *Nutrition* , 79–80, p. 110967.
- 1020 Szekely, Y. *et al.* (2020) “Spectrum of cardiac manifestations in COVID-19: A  
1021 systematic echocardiographic study,” *Circulation*. Ovid Technologies (Wolters  
1022 Kluwer Health), 142(4), pp. 342–353.
- 1023 Szklarczyk, D. *et al.* (2019) “STRING v11: protein-protein association networks  
1024 with increased coverage, supporting functional discovery in genome-wide  
1025 experimental datasets,” *Nucleic acids research*, 47(D1), pp. D607–D613.
- 1026 Tavazzi, G. *et al.* (2020) “Myocardial localization of coronavirus in COVID-19  
1027 cardiogenic shock,” *European journal of heart failure*, 22(5), pp. 911–915.
- 1028 Tran, D. H. and Wang, Z. V. (2019) “Glucose Metabolism in Cardiac  
1029 Hypertrophy and Heart Failure,” *Journal of the American Heart Association*,  
1030 8(12), p. e012673.
- 1031 Vastag, L. *et al.* (2011) “Divergent effects of human cytomegalovirus and  
1032 herpes simplex virus-1 on cellular metabolism,” *PLoS pathogens*, 7(7), p.  
1033 e1002124.
- 1034 Verma, A. *et al.* (2020) “A combinatorial approach of a polypharmacological  
1035 adjuvant 2-deoxy-D-glucose with low dose radiation therapy to quell the  
1036 cytokine storm in COVID-19 management,” *International journal of radiation*  
1037 *biology*. Informa UK Limited, 96(11), pp. 1323–1328.
- 1038 Wick, A. N. *et al.* (1957) “Localization of the primary metabolic block produced  
1039 by 2-deoxyglucose,” *The Journal of biological chemistry*, 224(2), pp. 963–969.
- 1040 Williamson, J. C. *et al.* (2016) “High-performance hybrid Orbitrap mass  
1041 spectrometers for quantitative proteome analysis: Observations and  
1042 implications,” *PROTEOMICS*, pp. 907–914. doi: 10.1002/pmic.201400545.
- 1043 Wiśniewski, J. R. *et al.* (2009) “Universal sample preparation method for  
1044 proteome analysis,” *Nature methods*, 6(5), pp. 359–362.
- 1045 Wong, S. L. A. *et al.* (2005) “In vivo functional characterization of the SARS-  
1046 Coronavirus 3a protein in Drosophila,” *Biochemical and biophysical research*  
1047 *communications*, 337(2), pp. 720–729.
- 1048 Xie, Y. *et al.* (2022) “Long-term cardiovascular outcomes of COVID-19,” *Nature*  
1049 *medicine*, 28(3), pp. 583–590.

1050 Yang, L. *et al.* (2021) "Cardiomyocytes recruit monocytes upon SARS-CoV-2  
1051 infection by secreting CCL2," *Stem cell reports*, 16(9), pp. 2274–2288.

1052 Yates, A. D. *et al.* (2020) "Ensembl 2020," *Nucleic acids research*, 48(D1), pp.  
1053 D682–D688.

1054 Yu, G. *et al.* (2012) "clusterProfiler: an R package for comparing biological  
1055 themes among gene clusters," *Omics: a journal of integrative biology*, 16(5),  
1056 pp. 284–287.

1057 Zhang, Y. *et al.* (2021) "SARS-CoV-2 hijacks folate and one-carbon metabolism  
1058 for viral replication," *Nature communications*, 12(1), p. 1676.

1059 Zhou, B. and Tian, R. (2018) "Mitochondrial dysfunction in pathophysiology of  
1060 heart failure," *The Journal of clinical investigation*, 128(9), pp. 3716–3726.

1061 Zhu, J.-Y. *et al.* (2021) "Functional analysis of SARS-CoV-2 proteins in  
1062 *Drosophila* identifies Orf6-induced pathogenic effects with Selinexor as an  
1063 effective treatment," *Cell & Bioscience*. doi: 10.1186/s13578-021-00567-8.

1064

1065

1066

1067

1068

1069

1070

1071

1072

1073

1074

1075

1076

1077

1078

1079

1080

1081 **FIGURE LEGENDS**

1082

1083 **Figure 1. SARS-CoV-2 *Nsp6*, *Orf6* or *Orf7a* transgene expression causes**  
1084 **developmental lethality, heart morphological and functional defects (A)**

1085 Schematic representation of the genetic screen to identify individual SARS-  
1086 CoV-2 genes with cardiac pathology. **(B)** Quantitation of mortality rate prior to  
1087 eclosion for each individually expressed SARS-CoV-2 gene from the crosses  
1088 in (A). Mortality calculated as (CyO wing – straight wing) / CyO wing × 100. **(C)**

1089 Graph displaying lifespan for adult flies carrying SARS-CoV-2 *Nsp6*, *Orf6*,  
1090 *Orf7a* or *Nsp3* transgene expression. *w*<sup>1118</sup> is a wild-type control. **(D)** The adult

1091 heart phenotype induced by *4XHand-Gal4*, cardioblast-specific overexpression  
1092 (OE) of the UAS-SARS-CoV-2 *Nsp6* transgene. Cardiac actin myofibers were  
1093 visualized by phalloidin staining. Dotted lines delineate the outline of the heart  
1094 tube. Arrow points to missing cardiac myofibers. *w*<sup>1118</sup> is a wild-type control.

1095 Scale bar = 40 μm. **(E)** Quantitation of adult heart cardiac myofibrillar density  
1096 relative to control. SARS-CoV-2 *Nsp6* (*4XHand-Gal4*) flies, and *w*<sup>1118</sup> is a wild-  
1097 type control. N=6 flies per genotype. **(F)** Schematic representation of heart

1098 diastolic and systolic diameter, and the heart period by optical coherence  
1099 tomography (OCT). **(G)** *Drosophila* heartbeat video images from flies induced

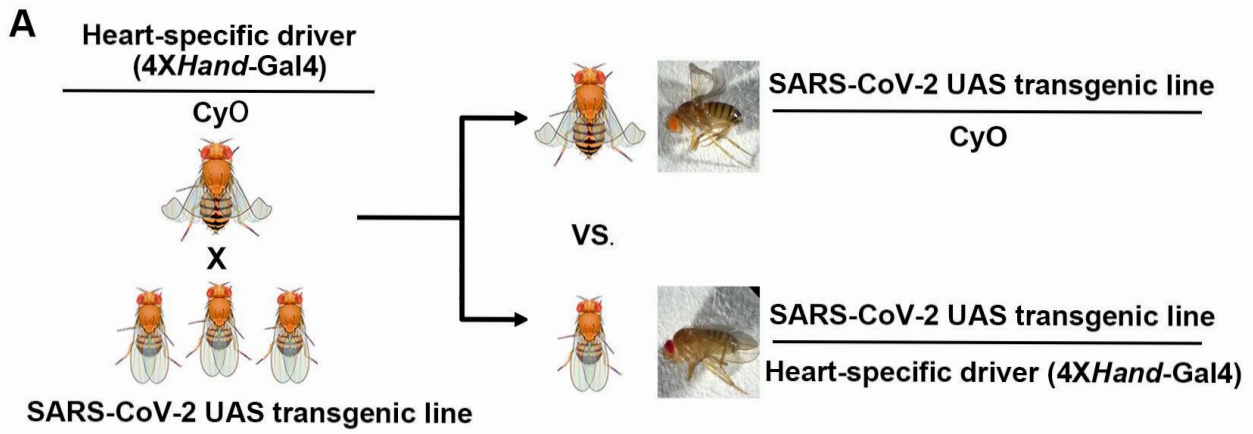
1100 by *4XHand-Gal4* cardioblast-specific overexpression (OE) of the UAS-SARS-  
1101 CoV-2 *Nsp6* transgene. *w*<sup>1118</sup> is a wild-type control. **(H)** Quantitation of adult

1102 heart diastolic diameter. N=10 flies per genotype. **(I)** Quantitation of heart  
1103 period, *i.e.* indication of heart rate. N=10 flies per genotype. Statistical

1104 significance (\*) defined as P < 0.05.

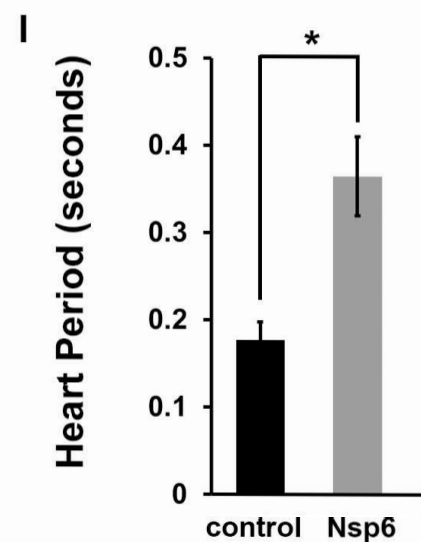
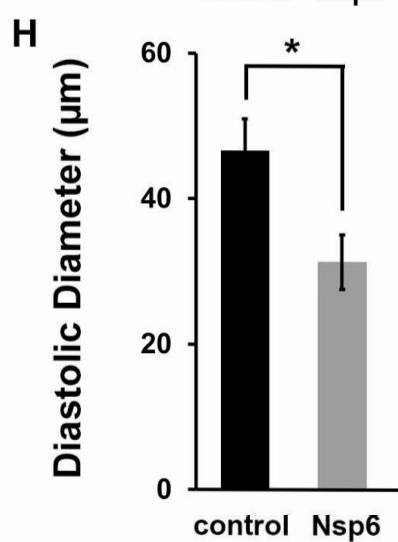
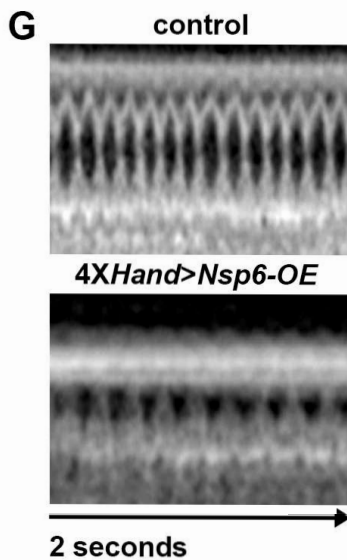
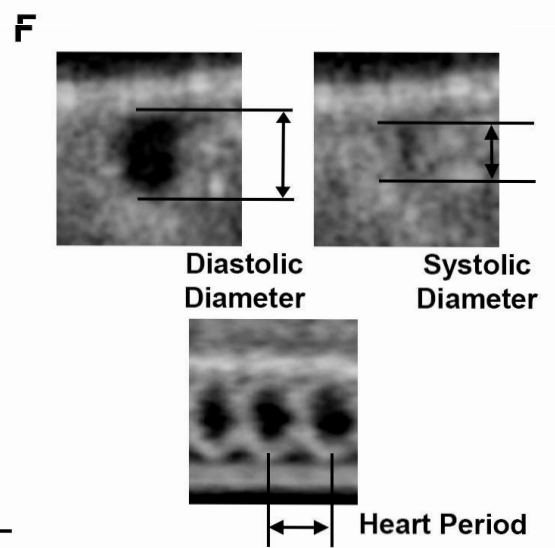
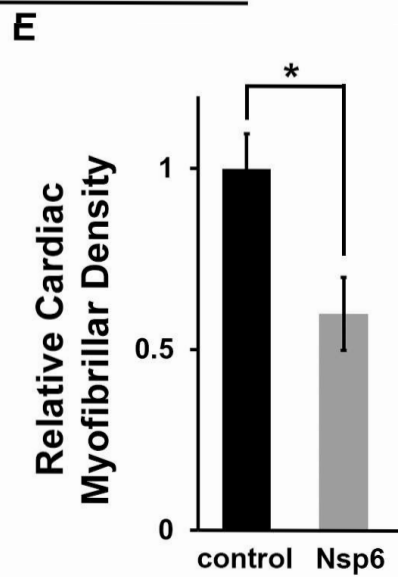
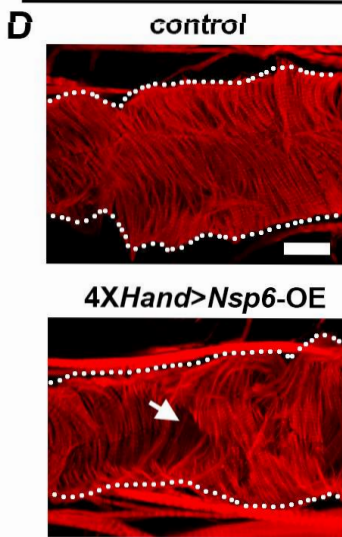
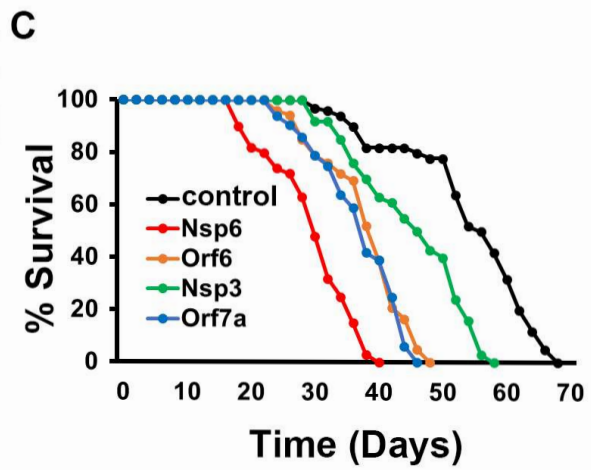
1105

**Figure 1**



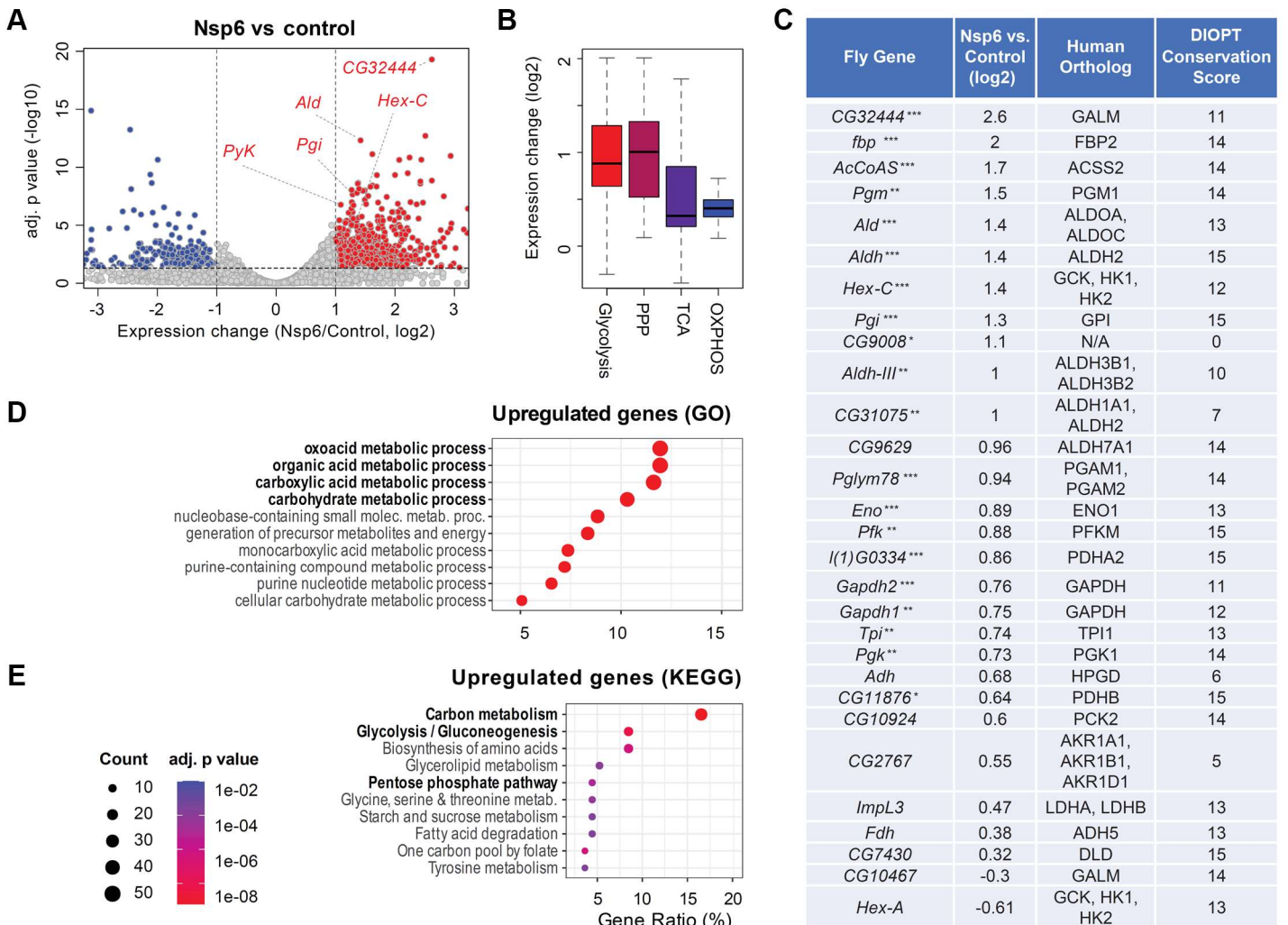
**B** Cross with 4XHand-Gal4/CyO

	CyO Wing	Straight Wing	Mortality
w <sup>1118</sup> (control)	108	108	0.0%
Nsp6	111	72	35.1%
Orf7a	111	78	29.7%
Orf6	105	76	27.6%
Nsp3	109	92	15.6%
Orf8	110	104	5.5%
Orf7b	106	102	3.8%
Orf9b	104	102	1.9%
Nsp1	103	102	1.0%
Orf3b	105	104	1.0%
Orf3a	110	109	0.9%
Orf10	104	104	0.0%
Nsp2	105	105	0.0%



1131 **Figure 2. SARS-CoV-2 *Nsp6* alters the expression of host glycolysis**  
1132 **genes in the fly heart (A)** Differential expression of fly heart genes upon  
1133 *4XHand-Gal4* cardioblast-specific transgenic overexpression (OE) of UAS-  
1134 *SARS-CoV-2 Nsp6*. X-axis: Gene expression differences between the *Nsp6*-  
1135 expressing heart versus wild-type control (*w<sup>1118</sup>*) in log2 scale. Y-axis: Adjusted  
1136 P values in -log10 scale. Each dot represents a gene: Red color denotes genes  
1137 upregulated in *Nsp6*-OE fly hearts; Blue color denotes genes downregulated in  
1138 *Nsp6*-OE fly hearts. **(B)** Box plot summarizes differentially expressed genes in  
1139 *SARS-CoV-2 Nsp6*-OE fly heart compared to wild-type control (*w<sup>1118</sup>*) heart,  
1140 involved in Glycolysis, Pentose Phosphate Pathway (PPP), TriCarboxylic Acid  
1141 cycle (TCA) and OXidative PHOSphorylation (OXPHOS). The top and bottom  
1142 of each box corresponds to the upper and lower quartiles, respectively. Each  
1143 thick line represents the median value. Whiskers indicate the largest, or  
1144 smallest, observations within 1.5 times of the interquartile range (upper-lower)  
1145 from the top / bottom of the boxes, respectively. **(C)** Gene expression changes  
1146 of fly glycolysis genes with their human orthologs. Orthology information and  
1147 conservation scores were obtained from DIOPT (max conservation score= 15)  
1148 (Hu *et al.*, 2011). \* adjusted P < 0.05, \*\* adjusted P < 0.01, \*\*\* adjusted P <  
1149 0.001. **(D-E)** Enrichment of genes with specific Gene Ontology (GO) terms (D)  
1150 or KEGG-defined pathways (E). Circle size: Number of genes associated with  
1151 the function. Color: Adjusted P values. X-axis represents the percentage of  
1152 genes with the function among all the significantly upregulated (adj. P value <  
1153 0.05) genes.  
1154  
1155

**Figure 2**



1181 **Figure 3. SARS-CoV-2 *Nsp6* increases glycolysis activity and heart-**  
1182 **specific *Pgi* overexpression causes heart morphological and functional**  
1183 **defects (A)** On the left, key metabolites in the glycolysis pathway. On the right,  
1184 quantitation of the enzymatic activity of Phosphoglucose isomerase (*Pgi*) and  
1185 NADH level in flies with ubiquitous (*Tub-Gal4* driver) overexpression of UAS-  
1186 SARS-CoV-2 *Nsp6* transgene or wild-type control (*w<sup>1118</sup>*). N=6 flies per  
1187 genotype. **(B)** Adult heart mitochondrial phenotype induced by *4XHand-Gal4*,  
1188 cardioblast-specific overexpression (OE) of the UAS-SARS-CoV-2 *Nsp6* or *Pgi*  
1189 transgenes. Cardiac actin myofibers were visualized by phalloidin staining.  
1190 Mitochondria were visualized by ATP5a antibody staining. Dotted lines  
1191 delineate the outline of the heart tube. Arrow points to missing mitochondria.  
1192 *w<sup>1118</sup>* is a wild-type control. Scale bar = 40  $\mu$ m. **(C)** Quantitation of percentage  
1193 of mitochondrial area in fly heart (see images in B). N=6 flies per genotype. **(D)**  
1194 *Drosophila* heartbeat video images from flies induced by cardioblast-specific  
1195 (*4XHand-Gal4* driver) overexpression (OE) of UAS-*Pgi* transgene. *w<sup>1118</sup>* is a  
1196 wild-type control. **(E)** Quantitation of adult heart diastolic diameter (in D). N=10  
1197 flies per genotype. **(F)** Quantitation of heart rate (in D). N=10 flies per genotype.  
1198 Statistical significance (\*) defined as  $P < 0.05$ .

1199

1200

1201

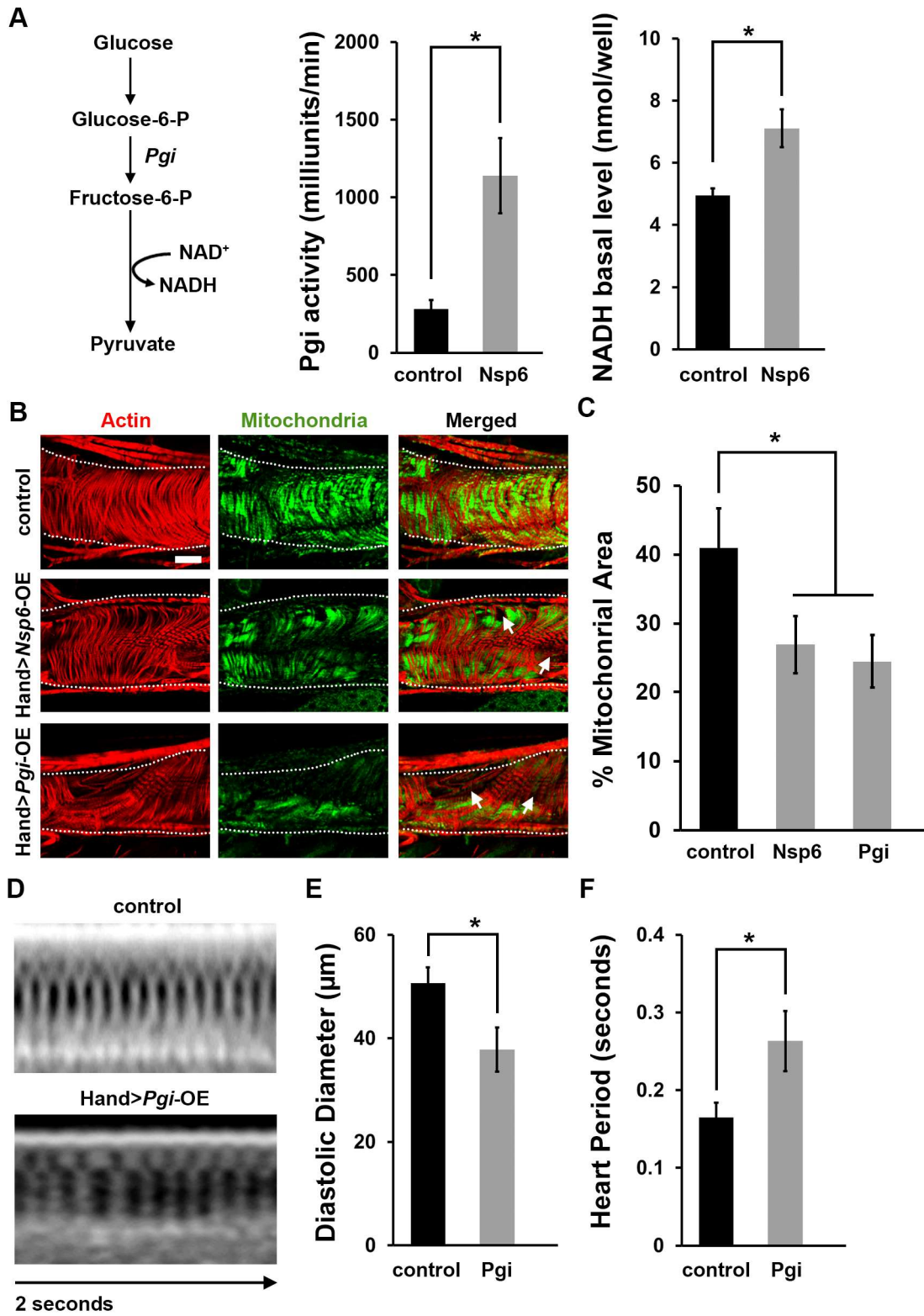
1202

1203

1204

1205

Figure 3



1231 **Figure 4. SARS-CoV-2 Nsp6 increases glycolysis gene expression by**  
1232 **inhibiting an MGA-containing repressive complex (A)** Heatmap  
1233 summarizes the abundance of transcription factors (obtained from mass  
1234 spectrometry analysis) in the mCherry (left) and SARS-CoV-2 *Nsp6* (right)  
1235 expressing HEK 293T cells. **(B)** Known protein-protein interactions among  
1236 SARS-CoV-2 *Nsp6*-binding transcription factors, as well as MYC and MAX.  
1237 Solid line: Interaction identified in this study. Dotted line: Other known  
1238 interactions from the STRING database (Szklarczyk *et al.*, 2019). **(C)**  
1239 Schematic illustration depicting regulation of glycolysis gene expression by  
1240 MGA or MYC-containing protein complexes. **(D-E)** Quantitation of the  
1241 enzymatic activity of Phosphoglucose isomerase (Pgi) (D) and NADH (E) levels  
1242 in flies with ubiquitous (*Tub-Gal4* driver) expression of the UAS-*Myc* transgene  
1243 or wild-type control (*w<sup>1118</sup>*). N=6 flies per genotype. Statistical significance (\*)  
1244 defined as  $P < 0.05$ . MGA, MAX gene-associated protein; MAX, MYC-  
1245 associated factor X; MYC, MYC proto-oncogene, basic helix-loop-helix (BHLH)  
1246 transcription factor; PCGF6, Polycomb group ring finger 6; TFDP1,  
1247 Transcription factor Dp-1.

1248

1249

1250

1251

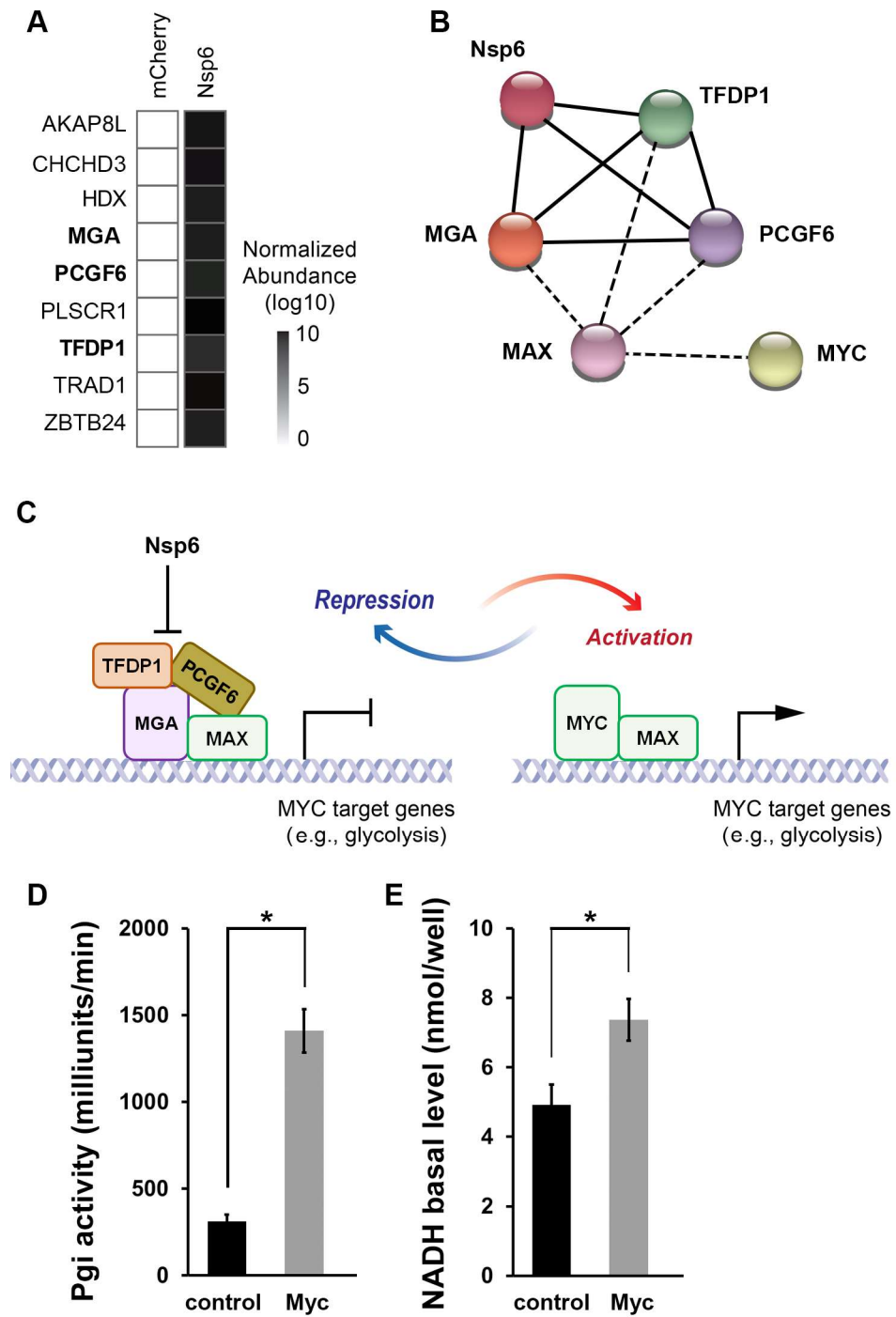
1252

1253

1254

1255

**Figure 4**



1281 **Figure 5. Inhibiting glycolysis activity by 2DG attenuates SARS-CoV-2**  
1282 **Nsp6-induced heart morphological and functional defects (A)** On the left,  
1283 key metabolites in the glycolysis pathway, with the conversion steps inhibited  
1284 by 2-deoxy-D-glucose (2DG) indicated. On the right, graph displays  
1285 quantitation of mortality rate prior to eclosion induced by cardioblast-specific  
1286 (*4XHand-Gal4* driver) overexpression of the UAS-SARS-CoV-2 *Nsp6*  
1287 transgene, or wild-type (*w<sup>1118</sup>*) control, following different doses of 2DG.  
1288 Mortality calculated as (CyO wing – straight wing) / CyO wing × 100. N=4  
1289 repeats. **(B)** Adult heart phenotype induced by cardioblast-specific (*4XHand-*  
1290 *Gal4* driver) overexpression (OE) of the UAS-SARS-CoV-2 *Nsp6* transgene,  
1291 compared to wild-type (*w<sup>1118</sup>*) control, following different doses of 2DG. Cardiac  
1292 actin myofibers were visualized by phalloidin staining. Dotted lines delineate  
1293 the outline of the heart tube. Arrow points to missing cardiac myofibers. Scale  
1294 bar = 40 μm. **(C)** Quantitation of adult heart cardiac myofibrillar density (in B)  
1295 relative to control. N=6 flies per genotype. **(D)** *Drosophila* heartbeat video  
1296 images from flies carrying cardioblast-specific (*4XHand-Gal4* driver)  
1297 overexpression (OE) of the UAS-SARS-CoV-2 *Nsp6* transgene, or wild-type  
1298 (*w<sup>1118</sup>*) control flies, following different doses of 2DG. **(E)** Quantitation of heart  
1299 rate (in D). N=10 flies per genotype. Statistical significance (\*) defined as P <  
1300 0.05.

1301

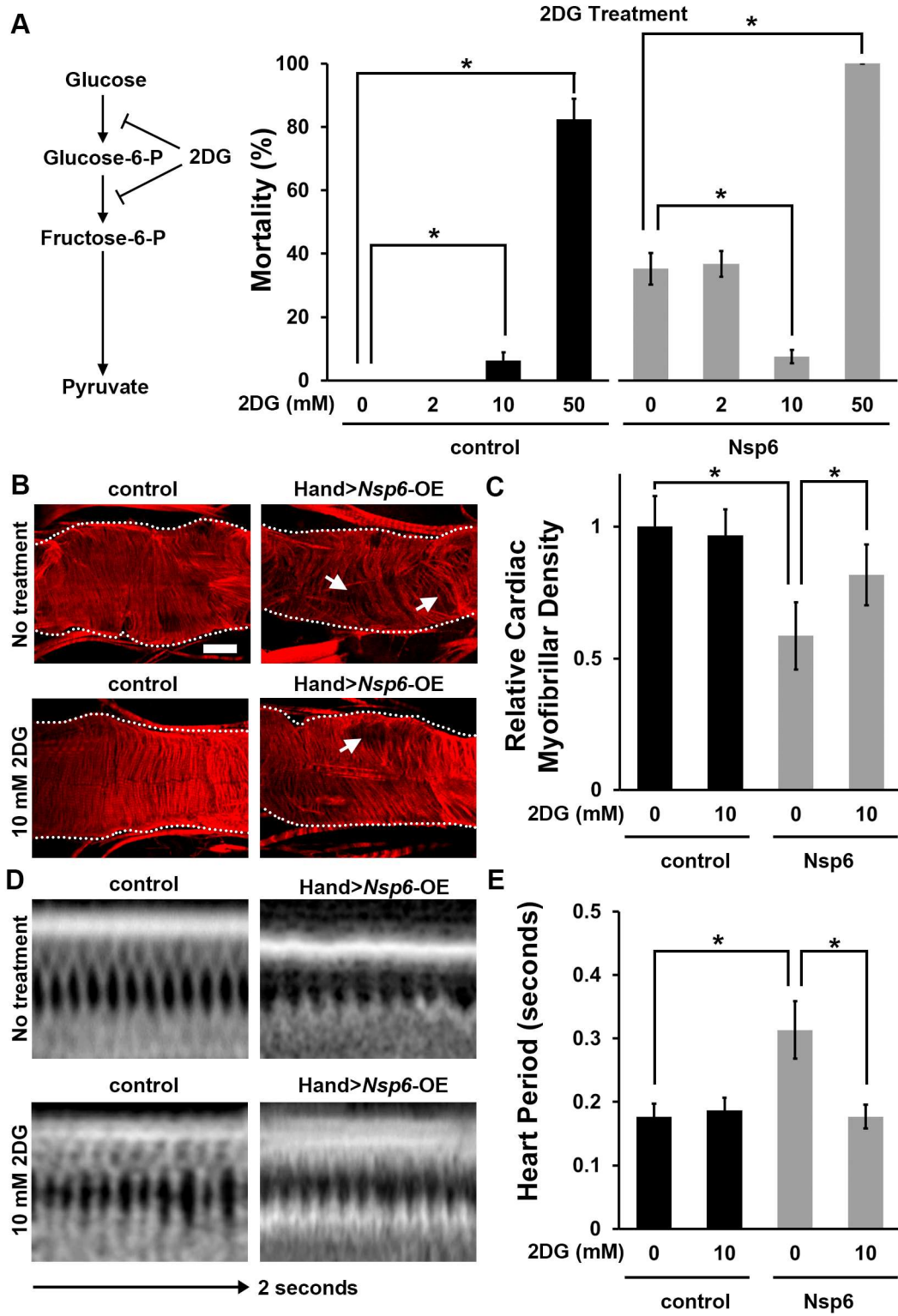
1302

1303

1304

1305

Figure 5



1331 **Figure 6. Inhibiting glycolysis activity by 2DG attenuates SARS-CoV-2**  
1332 **Nsp6-induced heart hypertrophy and functional defects in mouse primary**  
1333 **cardiomyocytes (A)** Mouse primary cardiomyocytes were transfected with  
1334 *SARS-CoV-2 Nsp6* transgene. The *SARS-CoV-2 Nsp6* transgene was  
1335 visualized in red. Lipofectamine only treated mouse primary cardiomyocytes  
1336 (Lipo) served as control. **(B)** Quantitation of hypertrophy markers *ANP* and *BNP*  
1337 relative to control. *ANP*, *Atrial natriuretic peptide*; *BNP*, *type B natriuretic*  
1338 *peptide*. N=2 per genotype. **(C)** On the left, key metabolites in the mammalian  
1339 glycolysis pathway. Graphs on the right, quantitation of the glycolysis gene  
1340 expression levels in mouse primary cardiomyocytes transfected with *SARS-*  
1341 *CoV-2 Nsp6* transgene, or lipofectamine (Lipo) control mouse primary  
1342 cardiomyocytes. N=2 per genotype. **(D)** Mouse primary cardiomyocyte  $Ca^{2+}$   
1343 wave video images from cells transfected with the *UAS-SARS-CoV-2 Nsp6*  
1344 transgene, or lipofectamine (Lipo) control mouse primary cardiomyocytes. **(E)**  
1345 Quantitation of the  $Ca^{2+}$  wave rate (in D). N=5 cells per genotype. Statistical  
1346 significance (\*) defined as  $P < 0.05$ .

1347

1348

1349

1350

1351

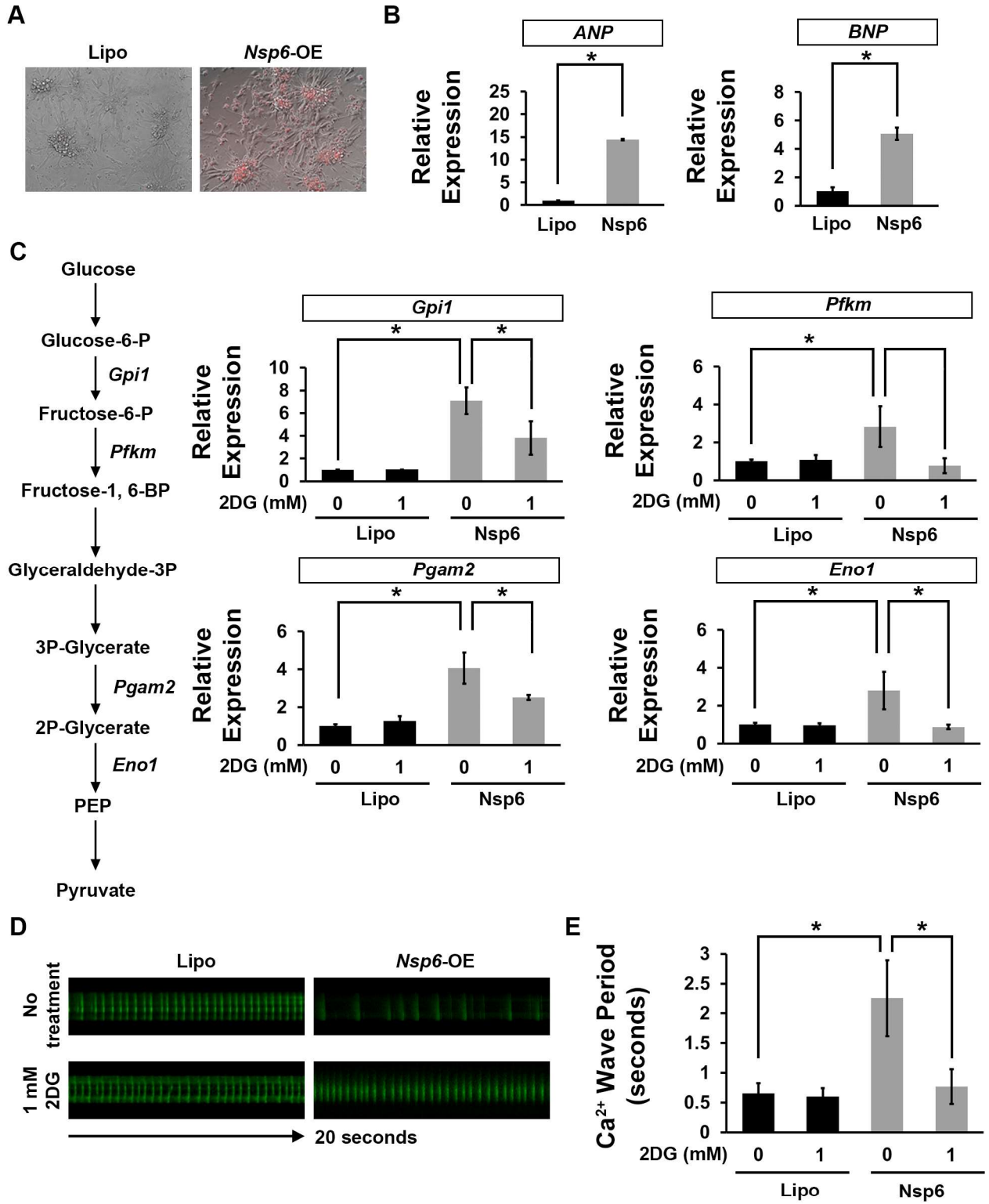
1352

1353

1354

1355

Figure 6



1381 **Figure 7. Model of SARS-CoV-2 Nsp6-mediated disruption of glycolysis**

1382 Graphic depiction of proposed model by which SARS-CoV-2 Nsp6 disrupts the  
1383 MGA/MAX:MYC/MAX balance thereby increasing glycolysis pathway activity,  
1384 which in turn leads to heart failure and potentially facilitates virus replication.  
1385 The model also indicates where 2-deoxy-D-glucose (2DG) might intervene and  
1386 inhibit the Nsp6-glycolysis-induced cardiac phenotype. MGA, MAX gene-  
1387 associated protein; MAX, MYC-associated factor X; MYC, MYC proto-  
1388 oncogene, basic helix-loop-helix (BHLH) transcription factor; PCGF6,  
1389 Polycomb group ring finger 6; ROS, reactive oxygen species; TCA cycle,  
1390 tricarboxylic acid cycle (a.k.a. Krebs cycle); TFDP1, Transcription factor Dp-1;  
1391 Hex-A/Hex-C, Hexokinase-A/-C; Phosphoglucose isomerase (Pgi).

1392

1393

1394

1395

1396

1397

1398

1399

1400

1401

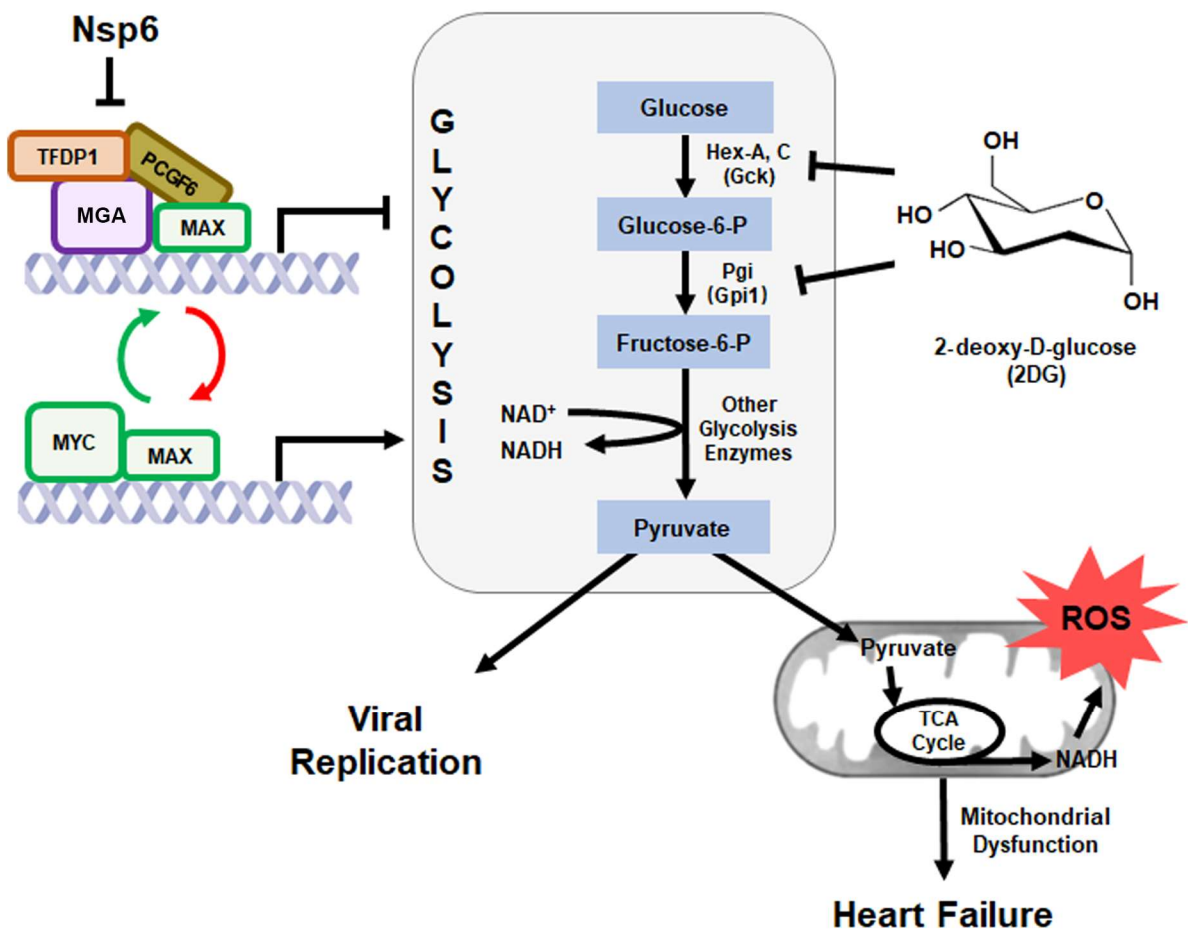
1402

1403

1404

1405

Figure 7



1431 **SUPPLEMENTAL INFORMATION**

1432

1433 **Supplemental Figure S1. Fly progeny from UAS SARS-CoV-2 crosses for**  
1434 **mortality at eclosion assay** Images of adult progeny emerging from pupa  
1435 stage from the crosses in Figure 1A, distinguished by carrying the balancer  
1436 (CyO curly wing; no viral transgene expression) or with the expression of the  
1437 SARS-CoV-2 gene driven by the heart-specific driver *4XHand*-Gal4 (straight  
1438 wing). *w*<sup>1118</sup> is a wild-type control.

1439

1440 **Supplemental Table S1. Differentially expressed genes in SARS-CoV-2**  
1441 **Nsp6 expressing fly heart (summary data for RNA-seq)**

1442

1443 **Supplemental Table S2. Host proteins (HEK 293T cells) interacting with**  
1444 **SARS-CoV-2 Nsp6 as identified by mass spectrometry**

1445

1446 **Supplemental Table S3. Primer sequences used for RT-PCR in mouse**  
1447 **primary cardiomyocytes**

1448

## Supplementary Files

This is a list of supplementary files associated with this preprint. Click to download.

- [supldataNsp6MGA2DG.pdf](#)